The Relationship Between Permeability, Porosity, and Microstructure in Vesicular Basalts

by

Martin O. Saar

a Thesis

Presented to the Department of Geological Sciences
and the Graduate School of the University of Oregon
in partial fulfillment of the requirements
for the degree of
Master of Science

June 1998

"The Relationship Between Permeability, Porosity, and Microstructure in Vesicular Basalts," a thesis prepared by Martin O. Saar in partial fulfillment of the requirements for the Master of Science degree in the Department of Geological Sciences. This thesis has been approved and accepted by:

_____

Dr. Michael Manga, Chair of the Examining Committee

_____

Date

Committee in charge: Dr. Michael Manga
                     Dr. Katharine Cashman
                     Dr. Eugene Humphreys

Accepted by:

_____

Vice Provost and Dean of the Graduate School

An Abstract of the Thesis of

Martin O. Saar for the degree of Master of Science in the

Department of Geological Sciences to be taken June 1998.

Title:

The Relationship Between Permeability, Porosity,

and Microstructure in Vesicular Basalts

Approved:⎯⎯⎯⎯⎯⎯⎯⎯⎯⎯⎯⎯⎯⎯⎯⎯⎯⎯⎯⎯⎯⎯⎯⎯

Dr. Michael Manga

This thesis presents measurements of permeability, k, porosity, ϕ, and microstructural parameters of vesicular basalts. Measurements are compared with theoretical models. A percolation theory and a Kozeny-Carman model are used to interpret the measurements and to investigate relationships between porosity, microstructure, and permeability.

Typical permeabilities for vesicular basalts are in the range of $10^{-14} < k < 10^{-10}$ m^2. Best permeability estimates, following power laws predicted by percolation theory, are obtained when samples are used that show "impeded aperture widening" due to rapid cooling and no bubble collapse (scoria and some flow samples). However, slowly cooled diktytaxitic samples contain elongated, "collapsed" bubbles. Measurements indicate that the vesicle pathway network remains connected and preserves high permeabilities. Image-analysis techniques are unsuccessful if used for Kozeny-Carman equation parameter determination for vesicular materials, probably because the average interbubble aperture size that determins k is not resolved with such a technique.

Curriculum Vita

NAME OF AUTHOR: Martin O. Saar

PLACE OF BIRTH: Stuttgart, Germany

DATE OF BIRTH: January 15, 1972

GRADUATE AND UNDERGRADUATE SCHOOLS ATTENDED:

University of Oregon
Albert-Ludwigs Universität, Freiburg, Germany

DEGREES AWARDED:

Master of Science in Geology, 1998, University of Oregon, U.S.A.
Vordiplom in Geology, 1995, Albert-Ludwigs Universität, Freiburg, Germany
Abitur, 1991, Wirtemberg Gymnasium, Stuttgart, Germany

PROFESSIONAL EXPERIENCE:

Research Assistant, Department of Geological Sciences,
    University of Oregon, Eugene, 1997-98

Teaching Assistant, Department of Geological Sciences,
    University of Oregon, Eugene, 1998

Hilfswissenschaftler (Research Assistant), Geologisches Institut,
    Albert-Ludwigs Universität, Freiburg, Germany, 1995-96

Geology Internship with UMT, Umwelt Meßtechnik GmbH (Environmental
    Measuring Technique Ltd.), Stuttgart, Germany, 3 months, spring 1993

AWARDS AND HONORS:

Staples Fellowship for outstanding scholastic achievements,
    University of Oregon, 1997

Acknowledgements

Contents

List of Figures

List of Tables

Chapter 1

Introduction

The flow of fluid through a porous material is governed by geometrical properties such as the porosity ϕ, the connectedness and tortuosity of the pore space, as well as properties of the flowing liquid. The flux is proportional to the applied pressure gradient driving the flow and the constant of proportionality is called Darcy's constant or the permeability $\mathbf{k}$, which is a second rank tensor and has the dimensions of length squared. Permeability is a measure of how easily a fluid flows through a porous medium and it therefore determines the rate of fluid flow through a material. The geometrical properties and not the properties of the fluid (density, viscosity) determine the intrinsic permeability $\mathbf{k}$ of a porous medium. Permeability is an important property for studies of ground water flow and remediation, contaminant migration, retrieval of geothermal energy, enhanced gas/oil recovery strategies, formation of ore deposits, mechanisms of faulting, degassing processes in volcanoes (e.g. Klug et al., 1996] and lava flows, storage of toxic and radioactive waste, and hydrothermal circulation at mid-ocean ridges.

The empirically derived equation that describes flow in porous material is called Darcy's Law [Darcy, 1856] and is usually written in the form

$$\mathbf{u} = -\frac{\mathbf{k}}{\mu} \cdot (\nabla P + \rho \mathbf{g} \nabla \zeta) , \tag{1.1}$$

where μ is the dynamic fluid viscosity, ∇P the applied pressure gradient, and $\mathbf{u}$ Darcy's velocity, the fluid flux, $\mathbf{Q}$, per cross sectional area, A, i.e. $\mathbf{u} = \mathbf{Q}/A$. The term $\rho \mathbf{g} \nabla \zeta$ is the elevation head at a height ζ above an arbitrary datum, fluid density ρ and gravitational acceleration $\mathbf{g}$.

Calculating permeability for given pathway geometries and porosities, ϕ, is useful when direct permeability measurements are expensive, difficult, or impossible to carry out. By contrast, porosities are generally easier and faster to determine and can even be done if only an image of a homogeneous sample is available. This can be the case for example when the permeability of a fracture system, now filled with secondary minerals, or the permeability of a partial melt system is of interest. The goal is therefore to find a relationship between porosity ϕ and permeability $\mathbf{k}$. This has been attempted since the early work of Rose [1945], who suggested a power-law relation between permeability and porosity, and later Kozeny and Carman [Carman, 1956; Dullien, 1979] and others [e.g. Berryman et al., 1987; Katz et al., 1986; Johnson et al., 1986]. Roberts et al. [1997] provide a recent review of several permeability estimation techniques. Most studies have focused on sedimentary rocks, and few investigations have concentrated on vesicular igneous rocks, despite their possible importance for contaminant storage and release (e.g. Hanford radioactive waste in the Columbia River Basalts) or as aquifers [e.g. Ingebritsen et al., 1993; Manga, 1996, 1997].

Since two porous materials with the same total porosity can have very different permeabilities, it is clear that there is no simple porosity-permeability relation [e.g. Cloud, 1941]. Other microstructural parameter like pore shape, pore space connectedness, and pathway tortuosity must also be considered.

In this thesis I compare the measured permeability of vesicular basalts with the predictions of theoretical models for given porosities and microstructural properties.

The goal is to find a porosity-microstructure-permeability relationship for vesicular materials where fluids flow through permeable spheres (vesicles), in contrast to most studies that have focused on flow around impermeable particles in granular materials.

Aquifers and reservoirs often show dual porosities and permeabilities [e.g. Bai et al., 1993; Bear et al., 1993, p.158], with fractures governing fluid flow, and interfracture pores determining the rock's capacity for storage and release of contaminants and Carbon-14 loss into low-permeability zones by diffusion, leading to overestimations of groundwater ages [e.g. Sanford, 1996]. Rubble zones containing fractures are abundant in basalt flows in their top and bottom part, although they also can be observed in central regions of the flow [e.g. Sanford, 1996]. Because of the important role of fractures in determinating the overall fluid flow in a basalt flow aquifer it is generally impossible to upscale laboratory permeability measurements of interfracture cores to total aquifer permeability values [e.g. Brace, 1980; Clauser, 1992; Guéguen et al., 1996; Sánchez-Vila et al., 1996; Tidwell et al., 1997]. However, laboratory measurements are useful for contaminant storage and release (via diffusion) estimations or more scientific questions about porosity-pore-microstructure-permeability relations and in dual-permeability models [Bai et al., 1993].

Permeability measurements are made using a steady state gas permeameter. Techniques used here to study permeability-porosity relationships of vesicular basalts include image analysis (two-point correlation functions), percolation theory, Kozeny-Carman equations, and total and connected (effective) porosity measurements (using a gas expansion technique). I also use these measurements to obtain a better understanding of various magmatic processes associated with degassing.

Chapter 2

MEASUREMENT TECHNIQUES

In this Chapter I describe the rock sampling criteria that were applied in order to obtain the information needed to study how the microstructure and porosity of a vesicular material determine its intrinsic permeability. Further I outline the sample preparation and experimental methods that were used to determine the permeability, total porosity, and accesible (connected) porosity. Finally I describe the various image analysing techniques used to gain information about the vesicle geometries, necessary for permeability models introduced in Chapter 4, ϕ-k measurement interpretations in Chapter 5, and permeability estimation models in Chapter 6.

2.1 Sampling

The samples are taken from blocks of Holocene andesitic basalt flows and cinder cones in the Cascade Mountain Range (Oregon) and central and eastern Oregon. Figure 2.1 is a map showing the locations where the samples are collected and Table II.1 lists some of the sample location characteristics. The Aa flows show a typical diktytaxitic texture, which is described by Dickinson [1965, p.101] as "a rock texture of some olivine basalt in the nothwestern United States, that is characterized by numerous jagged, irregular vesicles bounded by crystals, some of which protrude into the cavities." The flows typically have a dense middle and highly fractured top and

bottom, and therefore can be expected to show dual porosities and permeabilities, where the unfractured middle parts show permeabilities that are significantly lower ($\sim 10^3$) than the overall permeability of the aquifer [e.g. Brace, 1980]. The cinder cones are formed during a fire fountain eruption when lava was spattered and dispersed into the air where it often cooled below ductile deformation temperatures. This rapid lava chilling conserved highly vesicular scoria containing subspherical pores. Cinder cones in the Cascades Mountain Range are often aligned along fault systems subparallel to the High Cascade Graben and are frequently associated with flows developing at different stages at the same vent.

The collected samples were selected to enable me to relate observations of microstructures within unfractured cores to physical properties of the macroscopic material structure. This sampling criteria does not necessarily provide a representative cross section of the basalt flows and cinder cones. Also, by drilling cores from blocks it is only possible to obtain the interfracture matrix permeability since the bulk of any fluid would flow through fractures which are most abundant in the top and the bottom part of basalt flows [e.g. Brace, 1980; Ingebritsen et al., 1993]. It is this matrix permeability and porosity however that may determine the rock's capacity for storage and release of contaminants by diffusion [e.g. Sanford, 1996]. Different bubble sizes and pathway geometries are observed in the samples which allows me to compare their characteristics to permeability measurements and estimations.

The relatively young, fresh rock samples show little or no signs of secondary mineralization or weathering. This is important because secondary mineralization would decrease the permeability **k** of the rock by filling the void space [e.g. Keller et al., 1979; Blackwell et al., 1988; Ingebritsen et al., 1993]. However, Blair et al. [1996] observe a good correlation between **k** measurements and calculations based on image analysis techniques, using two-point correlation functions even when 5% clay
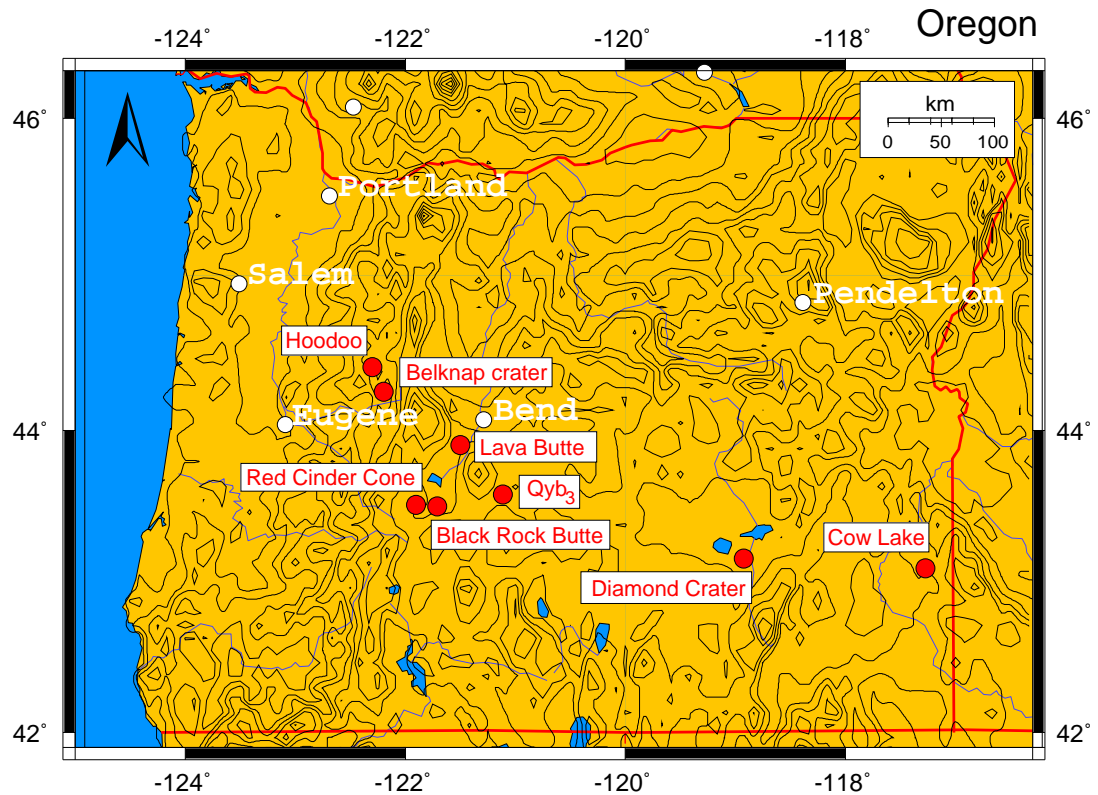
Figure 2.1: Sampling locations. Locations of samples in the Oregon Cascades, central and eastern Oregon. The scoria and basalt flow samples are collected from Hoodoo (scoria), Belknap crater (flow), Lava Butte (scoria, flow), Red Cinder Cone (scoria) Black Rock Butte (scoria, flow), Qyb_3 (flow), Diamond Crater (flow), Cow Lake (flow). Samples from Diamond Crater and Cow Lake are weathered and therefore not used.

Table II.1: Sampling locations and rock characteristics [Walker et al., 1991]

Name	Location	Type	Age	Characteristics
Hoodoo	HW 126 and HW 20 Cascades	scoria	Holocene	basaltic andesite, glassy texture, very vesicular
Belknap Crater	McKenzie Pass Cascades	flow	Holocene, 1,000 to 6,000 yr B.P. ^{14}C age	basaltic andesite & basalt flows and associated breccia, scoria if close to vent, flows show diktytaxitic texture, mainly Aa, some Pahoehoe flows
Lava Butte	at HW 97 south of Bend, OR	scoria, flow		
Qyb$_3$ Flow	north of Newberry Volcano, Cascades	flow		
Red Cinder Cone	short cut between HW 58 and HW 97, OR	scoria	Holocene, Pleistocene, Pliocene	basaltic and andesitic ejecta, unconsolidated, oxidized, fine to coarse grained, scoria and bombs
Black Rock Butte	short cut between HW 58 and HW 97, OR	scoria, flow	Pleistocene, Pliocene	scoria from mafic vent complex: basaltic andesite & basalt, flows show a diktytaxitic, aphyric to porphyric texture, flows form shields, lava cones and valley fill
Diamond Crater	Grand Malheur, SE Oregon	flow	Holocene	blocky and Pahoehoe structures, pressure ridges
Cow Lake	SE Oregon	flow	Holocene, younger than 6,800 yr ^{14}C age	basalt and basaltic andesite, blocky and Pahoehoe structures

Table 2.1:

7

is present in the sandstone samples. This might be expected because image analysis does not distinguish between the original rock and the clay which is the case for the fluid as well. Using ϕ_t-**k** relationships on the other hand would probably result in a larger inaccuracy since the densities of the rock and the clay are different, yielding an apparent porosity higher than the true total porosity ϕ_t. I expect secondary minerals to have a similar effect as clays.

2.2 Permeability Measurement

The flow of an incompressible, Newtonian fluid is described by the Navier-Stokes equations

$$\rho \left(\frac{\partial \mathbf{u}}{\partial t} + \mathbf{u} \cdot \nabla \mathbf{u} \right) = \rho \mathbf{g} - \nabla P + \mu \nabla^2 \mathbf{u}, \tag{2.1}$$

$$\nabla \cdot \mathbf{u} = 0. \tag{2.2}$$

If viscous forces resisting flow dominate over inertial forces, the non-linear term on the left-hand side of Equation (2.1) (Euler's equation) can be neglected and Equation (2.1) reduces to the Stokes equations

$$\mu \nabla^2 \mathbf{u} - \nabla P + \rho \mathbf{g} = \mathbf{0}, \tag{2.3}$$

$$\nabla \cdot \mathbf{u} = 0. \tag{2.4}$$

Stokes flow holds true only if the Reynolds number

$$Re = \frac{\rho u d}{\mu}, \tag{2.5}$$

where ρ is the density and μ the dynamic viscosity of the fluid, is smaller than 10^3 for a smooth tube with a characteristic diameter d. In natural samples, e.g. vesicular basalts, the fluid flows through tortuous, narrowing and opening pathways making the flow polydirectional at narrow passages where the flow velocity increases. In

addition rough side walls introduce disturbances. Therefore in a cylinder of porous material containing permeable bubbles of average diameter d, cross sectional area A, and porosity ϕ, the Reynolds number should ideally be smaller than one, for laminar flow to occur [Bear, 1988, p.177], and is given by

$$Re = \frac{\rho Q d}{\mu A \phi}. \tag{2.6}$$

Darcy's law is only valid when laminar and steady flow can be assumed. A small pressure gradient therefore has to be applied requiring sensitive pressure and flowrate transducers.

The elevation head in Equation (1.1) can be neglected, because of the low air density $\rho \approx 1.29$ kg/m^3 [Tipler, 1991] and a maximal sample length of $L_{max} = 23$ cm, i.e. $\rho \mathbf{g} \nabla \zeta \approx 0$. Assuming that the material is isotropic simplifies the permeability tensor $\mathbf{k}$ to a scalar k, which will be used hereafter. For an applied pressure gradient in x-direction, Equation (1.1) then becomes

$$u = -\frac{k}{\mu} \frac{\partial P}{\partial x}. \tag{2.7}$$

The permeability k is measured using Equation (2.7) in the form

$$k = \frac{Q}{\Delta P} \frac{\mu L}{A}, \tag{2.8}$$

where ΔP is the pressure difference across the sample cylinder of length L and cross sectional area A. The dynamic fluid viscosity of air at ambient temperature, about 20°C, is $\mu = 1.8 \times 10^{-5}$ Pa s [Tipler, 1991].

Measurements have to be made when both the air flow through the sample and the pressure gradient have reached a steady state. The time necessary to reach equilibrium due to pressure diffusion depends on the permeability of the rock. The pressure diffusion time, t_d, depends on the sample length L,

$$t_d \propto \frac{L^2}{\kappa}, \tag{2.9}$$

9

where

$$\kappa = k\frac{c_i^2 \rho}{\mu \phi}, \tag{2.10}$$

c_i is the isothermal sound speed, ϕ the porosity, ρ and μ the density and the viscosity of the fluid (here air) respectively [Phillips, 1991, p. 80-83]. κ can be interpreted as the diffusivity of pressure. The pressure diffusion time is therefore given by

$$t_d = \frac{L^2 \mu \phi}{k c_i^2 \rho}. \tag{2.11}$$

Samples with low k or longer cylinder length L take longer to reach a constant flow rate due to longer pressure diffusion times, Equation (2.11). Pressure differences, ΔP, and flowrates, Q, are therefore recorded by a personal computer at appropriate time intervals (0.5 to 2 s). Steady state is achieved when ΔP and Q values stop changing.

Especially for high flow rates, necessary to generate a measurable ΔP, Re is not smaller than 1 and inertial effects cannot be neglected. The ΔP-Q curve then is not linear, see Figure 2.2. To account for inertial effects, several sets of ΔP, Q measurements are made at steady state conditions and are related by fitting a second order polynomial

$$\Delta P = aQ + bQ^2, \tag{2.12}$$

through the data, where a is a coefficient related to permeability [Bear, 1988]. Curves for higher flow velocities and therefore higher Re numbers show a larger inertial effect (greater curvature, see Figure 2.2b) than curves for a less pronounced inertial effect, see Figure 2.2a.

Since air is used as the test fluid it is necessary to correct for the compressibility of the gas as both the flux and the specific discharge (Darcy velocity) vary with pressure from one side of the sample to the other. The correction can be made by multiplying the obtained permeability value by $2P_2/(P_1+P_2)$ [Dullien, 1979]. However the applied

10
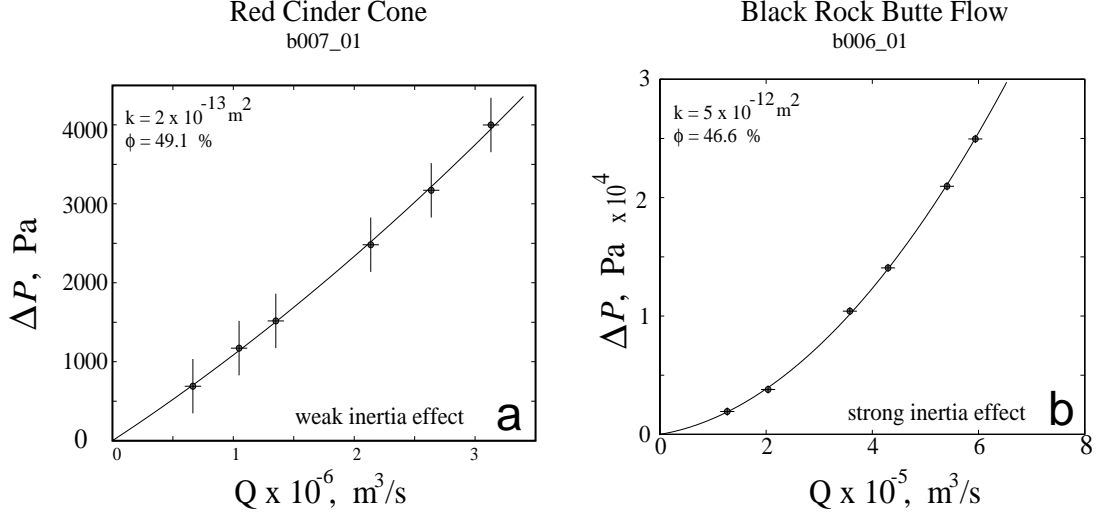
Figure 2.2: Inertial effects on permeability measurements. Inertial effects at Re not $\ll 1$ lead to a non-linear ΔP-Q relationship which is not assumed in Darcy's law. The inertia effect is more pronounced at high (**b**) flowrates (high fluid velocities) than at lower (**a**) flowrates, but is present at all fluid velocities. A curve fit and extraction of the linear term of the polynomial curve fit yields k, which is expressed by the slope of the curve.

pressures here are so low, (typically around 1 pound per square inch (PSI) ≈ 6.89 KPa) that this effect is minor.

Another correction is needed when the bubble diameter is comparable to the mean-free-path of the gas molecules flowing through the sample, as under these conditions it cannot be assumed that the fluid velocity at the walls is zero. Instead, a slip or drift velocity has to be taken into account, the so-called Klinkenberg effect [Dullien, 1979]. In basalt samples, however, bubble diameters are considerably larger than the mean-free-path of the air molecules used as the test fluid.

2.3 Core Preparation for Permeability Measurements

Cores are drilled from unfractured andesitic basalt blocks using a diamond drill attached to a lathe. The core diameter is 7.2 cm, and the length varies from 2 cm to 23 cm to ensure that the individual average bubble radius (the characteristic length scale) is significantly smaller than the core length, so that measurements average over statistically representative numbers of bubbles. Cores are dried in an oven at about 60°C for several hours to ensure one fluid (air) flow in the gas permeameter. Drying samples is easier than saturating the porous samples with water. After drying, the side walls of the cylindrical cores are sealed with impermeable tape so that air cannot enter or leave through the sidewalls and flow occurs along the long axis of the core.

2.4 Steady State Gas Permeameter

The permeameter (Figure 2.3) I built consists of an aluminum tube in which the prepared rock sample is attached, by securing an aluminum ring of 3 inch (7.62 cm) diameter to the uppermost end of the core by impermeable elastic tape. The ring itself is attached to the aluminum tube and the contact between tube and ring is sealed with tape, a hose clamp, and applied pressure (screws at the apparatus). This setup suspends the sample within the tube. The maximum applied gas pressure is P_1; atmospheric pressure is P_2.

The test fluid (air) is injected at ambient temperature (20°C) from the bottom, flows through the sample, and exits from the top of the cylinder into a tube which is attached to a flowmeter transducer (Honeywell Micro Switch Microbridge Mass Airflow Sensor AWM3100V). The pressure difference, $\Delta P = P_1 - P_2$, across the sample is measured by a pressure transducer (Honeywell Micro Switch Pressure Sensor 142PC05D)

at the bottom of the apparatus within the tube (P_1) and in some experiments at the top as well (P_2). However, early experiments have shown that P_2 is very close to atmospheric pressure and can therefore be assumed to be atmospheric pressure (101 KPa). Temperature is measured with J-type thermocouples next to the pressure transducers to enable correction for temperature variations. Different temperatures can occur as a result of room temperature fluctuations (approximately constant in the air-conditioned lab) and because of different compressions of air (temperature increases as pressure increases). However the temperature variations are extremely small for the induced small pressures ($\Delta P = P_1 - P_2 \approx P_1 - P_{atm}$, and $\Delta P_{max} \approx 7$ PSIG ≈ 48 KPa, usually below 1 PSIG ≈ 6.89 KPa) and viscosity variations of air due to temperature changes are thus minimal.

The air pressure within the sample decreases from the bottom (P_1) to the top ($P_2 \approx$ atmospheric pressure). The pressure outside the sample, but within the tube, is constant at P_1 (Figure 2.3). Therefore the pressure gradient across the tape at the very bottom of the sample is zero and increases upwards to almost ΔP_{max}. As a result, the tape is pressed against the sample due to the pressure difference across the tape which increases with increasing P_1. This setup provides an efficient seal as it presses the impermeable tape hardest towards the sample when the applied pressure P_1 is highest. The seal is tested by inserting an aluminum core in the permeameter and applying a maximum pressure of 60 PSI. The measured flowrate of zero indicates an efficient seal.

2.5   Total Porosity (ϕ_t) Measurement

The samples have a cylindrical shape which enables an easy calculation of their volume V. Total porosity therefore can be calculated when the matrix density ρ_m(rock without voids) is known. I determine ρ_m by powdering rocks to eliminate pore space,
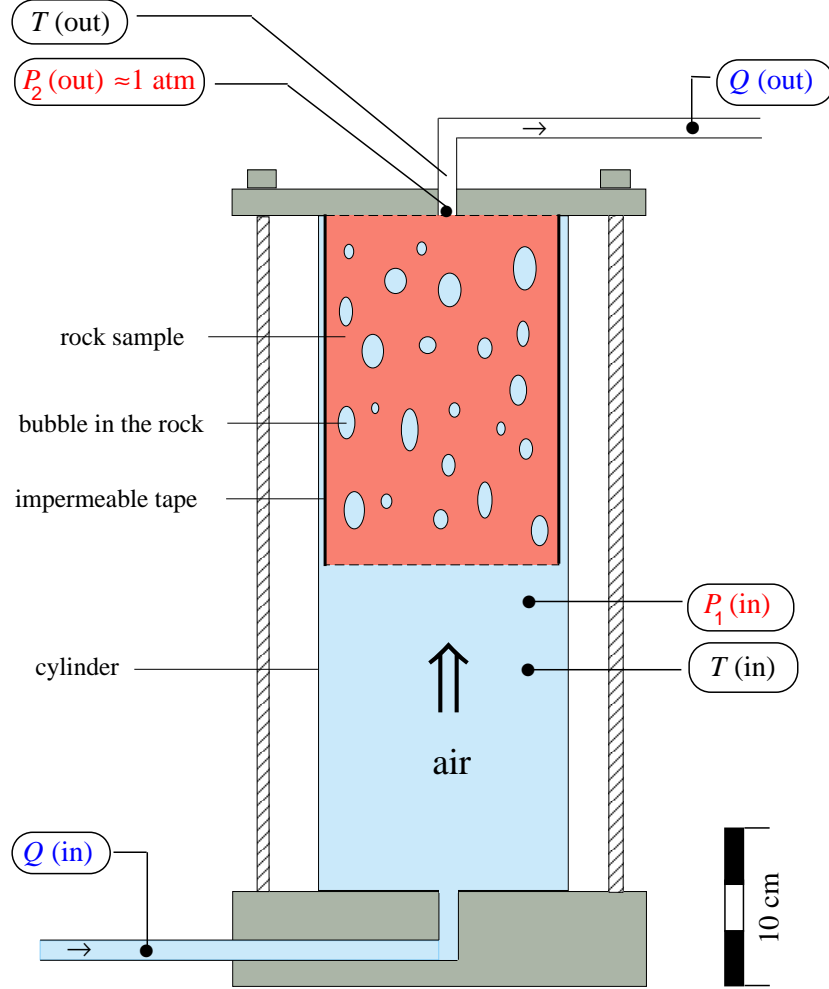
Figure 2.3: Steady state gas permeameter. The cylindrical sample is suspended at the top of the aluminum tube. Maximum pressure P_1 is applied below the sample within the tube. The pressure decreases within the sample and reaches approximately ambient (atmospheric) pressure P_2 at the permeameter outlet. The flowrate Q and the pressure difference ΔP have to reach a steady state before measurements are taken. The effects of inertia and compressibility of gases are corrected for. The Klinkenberg slip effect has not to be taken into account, because the mean-free-path of the air molecules is signifficantly smaller than the pore space.

adding water, and weighing the powder-water-mixture. Total porosity ϕ_t is calculated by

$$\phi_t = 1 - \frac{m}{\rho_m V}, \tag{2.13}$$

where m is the mass of the core with volume V. The matrix density ρ_m was obtained by grinding rock that was leftover from core drilling to eliminate voids. The powder was then placed in a graduated cylinder (volume = 250 ml ±2 ml) and a known amount of water (determined by weighing) was added. The density of the powder was then determined by weighing the full beaker. It is necessary to add water, since a known volume of powder contains an unknown amount of air-filled void space in between the grains. Filling this void space with a known amount of water (of known density) enables the matrix density determination. Intercrystalline micropores might not be completely eliminated during the grinding process. This reduces the matrix density in Equation (2.13) leading to an underestimation of the total porosity. This effect is probably more pronounced in the very crystalline (up to holocrystalline) basalt flow samples (Figure 3.4) than in the cinder cone (scoria) samples (Figure 3.2) which show a more glassy texture and therefore fewer micropores. The uncertainty of the total porosity measurement can be estimated by

$$\sigma_{\phi_t} = \sqrt{\left(\frac{\Delta m}{m}\right)^2 + \left(\frac{\Delta \rho_m}{\rho_m}\right)^2 + \left(\frac{\Delta V}{V}\right)^2} \tag{2.14}$$

and is $\sigma_{\phi_t} \approx 5\%$

2.6 Connected Porosity (ϕ_c) Measurement

The connected, also called accesible and effective, porosity is measured using a gas expansion technique (Figure 2.4). This is done by placing the sample[1] in a chamber

---

[1]The accessible porosity of the core samples is measured with the impermeable tape attached to the sidewall of the cylindrical samples since this is the configuration used for permeability measurements.
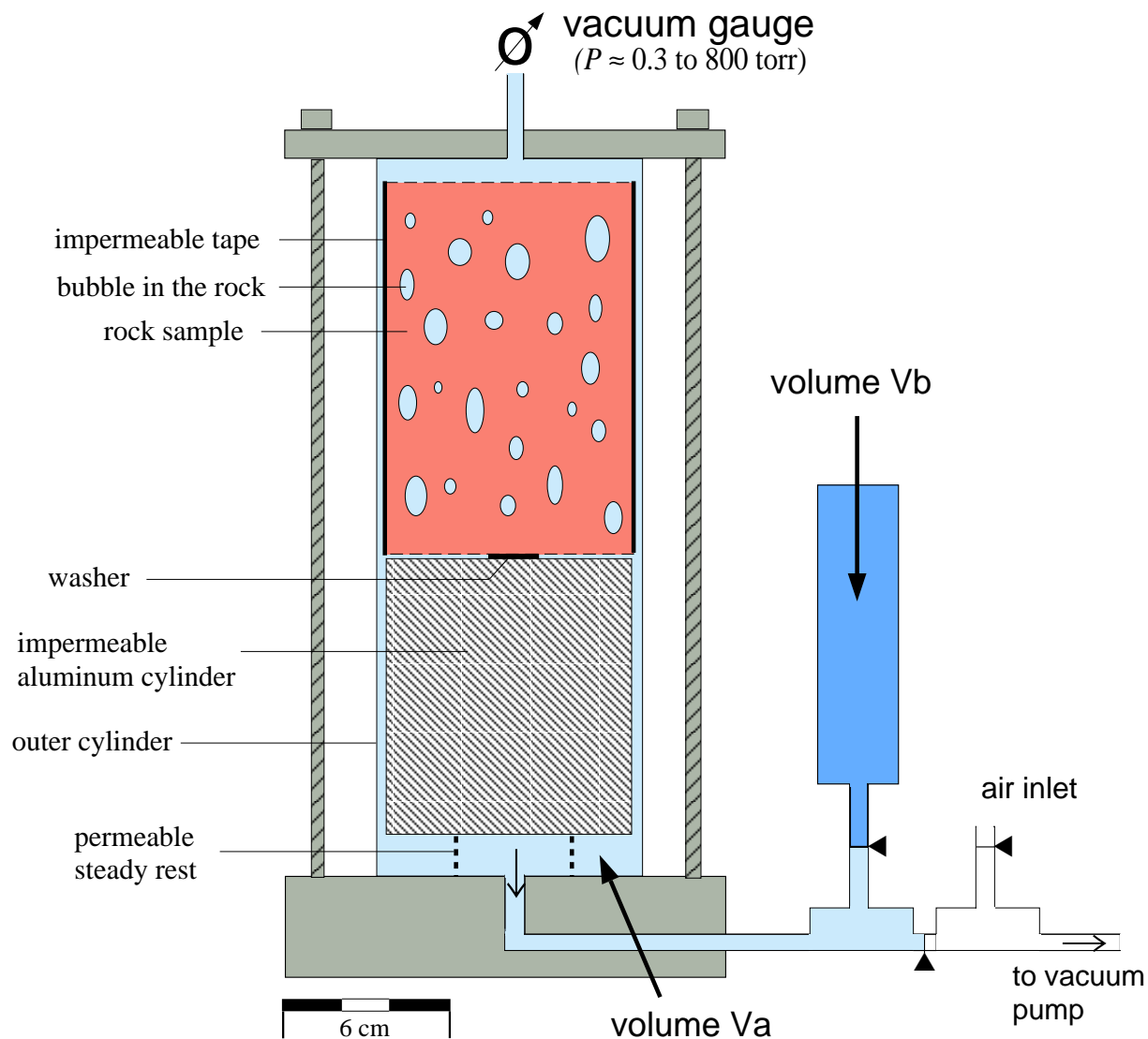
Figure 2.4: Air pycnometry: connected porosity measurements. Air pycnometry measurements are conducted to determine the accesible (connected) porosity of the samples. A vacuum is applied to chamber A. Then the valve between chamber A with pressure P_1 and B (with pressure P_2) is opened and the final pressure (P_f) of the system is recorded to calculate the connected porosity in Equation (2.15).

of known volume, V_A, to which a vacuum is applied. Then a valve is opened and air enters from a second chamber of known volume, V_B. This is often done with Helium. I use air as the test gas since the basalt samples have relatively big bubbles, and have been exposed to air. By comparing the pressure change in chamber A (P_1) and B (P_2) before the opening of the valve with the final pressure (P_f) of the total system after opening the valve, provides the connected porosity

$$\phi_c = 1 - \frac{V_A}{V_S} - \frac{V_B}{V_S}\left(\frac{P_f - P_2}{P_f - P_1}\right), \tag{2.15}$$

where:

V_S = total volume of the porous sample
V_A = volume of the empty vacuum chamber A
V_B = volume of the (ambient P) pressure chamber B
P_1 = minimum pressure in the vacuum chamber A
P_2 = pressure in the (ambient P) pressure chamber B
P_f = final equilibrium pressure in the system (A + B) with open valve

2.7   Comparison of Total and Connected Porosity

Total porosity measurements are expected to underestimate the true total porosity because the matrix density value is likely to be too low, especially for very crystalline basalt flow samples (see Chapter 3). The data points in Figure 2.5 therefore show the lower bound of total porosity. Measurements of the accessible porosity on the other hand are more likely to include connected intercrystalline micropores. If all pores are connected this leads to higher accessible than total porosity values, which cannot be the case. The data points in Figure 2.5 are therefore expected to plot more to the right of their current position which in general tends to move the data points onto the line $\phi_c = \phi_t$. All pores appear to be highly connected in vesicular basalts, that is $\phi_c \approx \phi_t$ (Figure 2.5).
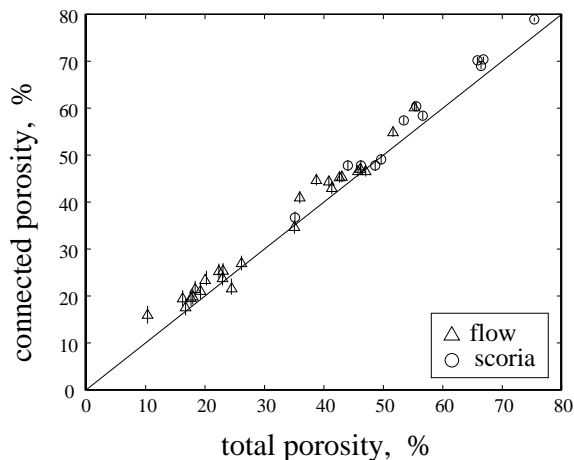
Figure 2.5: Total versus connected porosity. Accesible porosity appears to be higher in general than total porosity. An explanation for this result is given in the text. The uncertainty of ϕ_t is estimated by Equation (2.14) to be about $\sigma_{\phi_t} \approx 5\%$. Virtually all pores appear to be connected in vesicular basalts.

2.8   Image Analysis

Image analysis of the pore size and shape distribution is used to quantify the material's microstructure. This is important since permeability depends not only on porosity but also on microstructural parameters like pore shape, pore space connectivity, pathway size, and tortuosity.

Investigations of the samples' microstructure was studied using thin section and image analysis techniques. Thin sections give a more qualitative impression of the predominant structures of a small cross sectional area, whereas image analysis techniques allow quantitative investigations of a larger core cross section. For the latter I used two different approaches to gain different information: analysis of cross sec-

tional images first by an image analysis program (NIH Image)[2] and second by spatial correlation functions (SCF).

For both image analysis techniques it is necessary to prepare the core cross sectional discs for scanning purposes. The pores are first filled with spray paint to access very small pores and then with plaster to completely fill large voids. The surfaces are polished to eliminate surplus paint on non-void rock faces and then spray-painted with a clear lacquer to enhance the black (rock) and white (voids) contrast. The rock discs are then directly scanned at 1200 dpi resolution and inverted so that the voids are black and the rock is white to achieve a binary image. Figure 2.6 shows typical scanned images of three different kinds of rock samples. Images of all rock samples are provided in Appendix B.

2.8.1 NIH-Image Analysis

NIH-image is an image analysis program developed by the National Institute of Health (NIH) widely used to gain quantitative, statistical information about images. Here it is used to measure pore cross sectional area and pore circumference. The number of analyzed pores varies from 200 to over 2000 in each image, depending on the pore size distribution of the particular sample.

Characteristic areas A_c for each core were obtained by calculating the median vesicle area A_{50}. Figure 2.6 shows typical cumulative curves and A_{50} values for the three rock examples.

Relative roundness R_{round} was calculated by dividing the average circumference squared by the average characteristic area A_c of each bubble and then normalizing

---

[2]NIH-Image (version 1.61b8) of the National Institute of Health (NIH)

19

each value by such a value for a circle

$$R_{\text{round}} = \frac{P^2}{4\pi A_c}.$$ (2.16)

A perfectly circular pore has $R_{\text{round}} = 1$, whereas decreasing roundness is indicated by increasing R_{round}-values ($R_{\text{round}} > 1$). Figure 2.6 shows typical roundness distributions and values for the three rock types.

Porosities were not determined by the NIH-image analysis technique, because the total image area of which the pores were analyzed is not easily determined by the program. Porosity calculations based on image analysis techniques was carried out by one-point correlation functions (see following section).

2.8.2   Spatial Correlation Functions (SCF)

Spatial correlation functions (SCF) provide a means for the characterization of the microstructure of a two-phase medium, e.g. rock and pores [Berryman, 1985, 1987] and have been investigated with respect to permeability calculations using Kozeny-Carman equations [Carman, 1956; Dullien, 1979; Berryman et al., 1986, 1987; Blair et al., 1996]. Following the approach by Berryman [1985] and Blair et al. [1996], I use an indicator function f which is defined to be $f(\mathbf{x}) = 1$ if $\mathbf{x}$ is within a pore space and $f(\mathbf{x}) = 0$ if $\mathbf{x}$ is in the rock. The ascii-bitmap images obtained by scanning the prepared core discs contain only ones and zeros for voids and rock matrix respectively which represents the function f. After transforming the ascii-bmp file into a MATLAB[3] readable data file, it is straightforward to do matrix calculations needed for SCF-operations. I wrote a MATLAB program to generate a $a \times b$-matrix (a = width, b = height of the image) containing the ones and zeros and to do the

---

[3]MATLAB (R), version 5.2.0.3084, is a numeric computation and visualization software by Math-Works, Inc.

Lava Butte Cinder Cone   Lava Butte Flow   Black Rock Butte Flow

scanned core images

b020_2,3   b021_02   b013_01

median area, cm^2

$A_{50} = 0.019$ cm^2

$A_{50} = 0.076$ cm^2

$A_{50} = 0.067$ cm^2

bubble area, cm^2 bubble area, cm^2 bubble area, cm^2

number of bubbles

$R_{\mathrm{round}} = 1.39$

$R_{\mathrm{round}} = 1.37$

$R_{\mathrm{round}} = 2.29$

roundness R_{round} roundness R_{round} roundness R_{round}
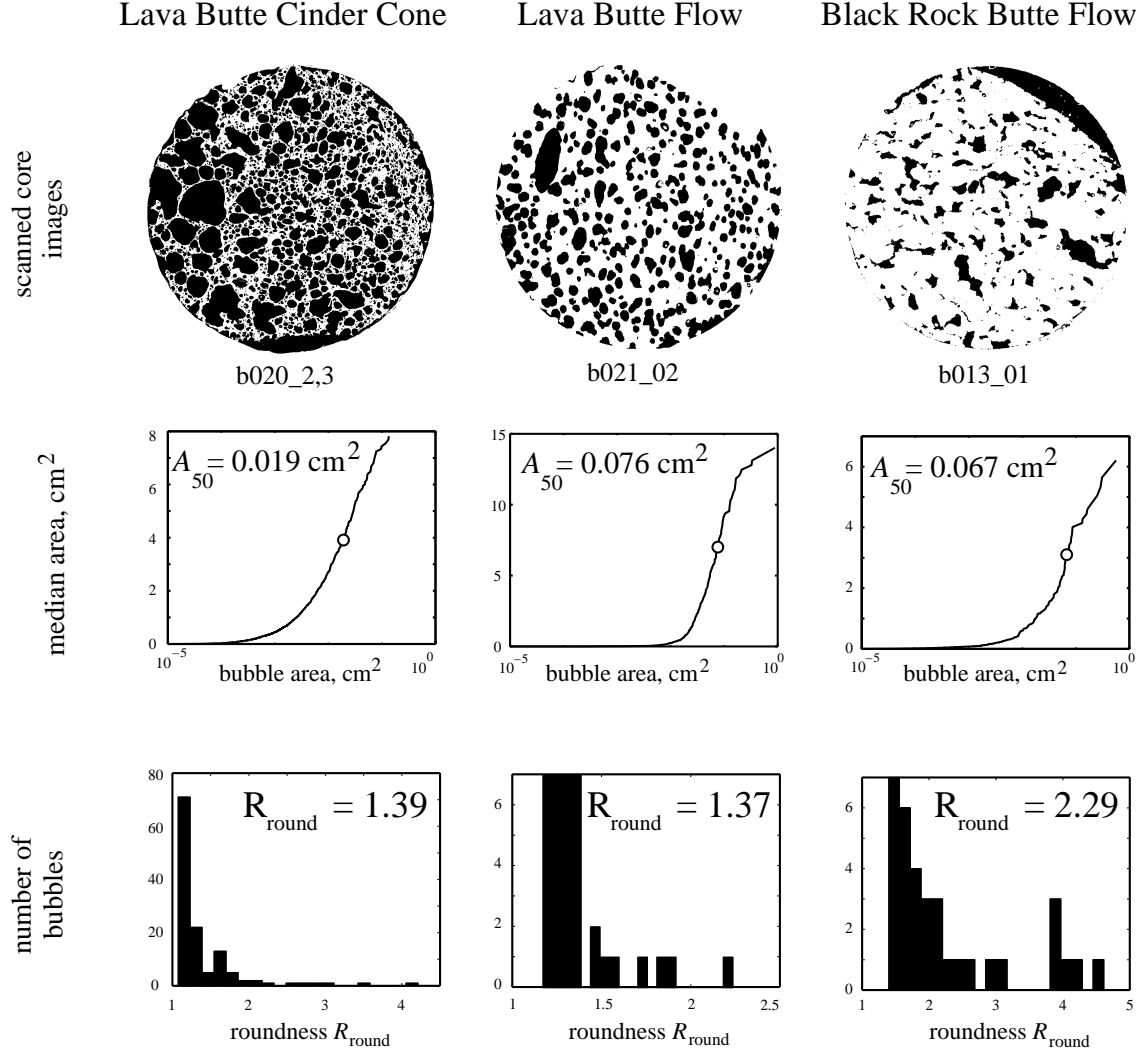
Figure 2.6: Comparison of microstructural characteristics of the three sample types. Determined using the NIH-image analysis technique (see Chapter 2). A_{50} is the median cross sectional bubble size and is refered to as the characteristic bubble area A_c. R_{round} is the average bubble roundness, where $R_{\mathrm{round}} = 1$ indicates a perfect sphere and $R_{\mathrm{round}} > 1$ measures distortion from a spherical shape.

SCF-calculations described below.

One-point correlation function (S_1)

The integral of f over the area of the image provides an estimate of the porosity of the sample, assuming that the rock is isotropic [Berryman, 1985, 1987; Blair et al., 1996]. This integral is also called the one-point correlation function S_1 and indicates the probability that any point lies in a pore space [Berryman 1985; Blair et al. 1996]. Determining the total porosity of a sample by one-point correlation functions provides only a rough estimate, since it uses only a fraction of the cross sectional area of the core for the calculation and does not integrate over the whole core, unlike the "powdering-weighing" method (described above). This problem can become even more severe, when the rocks are heterogeneous. However I can use the image analysis method to check the algorithm of the spatial correlation function on generated images of circles and ellipses and on relatively homogeneous rock samples.

Two-Point Correlation Functions (S_2)

Spatial correlation functions are also useful when they are done on two (S_2) or more (S_n) points. Two-point correlation functions S_2 are of special interest here, because they can be used to determine the specific surface area of a sample [Berryman, 1987]. In combination with S_1 to calculate the porosity of a sample they are a powerful technique because porosity and specific surface area can be used in Kozeny-Carman equations to estimate permeability [Carman, 1956; Dullien, 1979; Berryman et al., 1986, 1987; Blair et al., 1996] if a formation factor F is known. The formation factor is a measure of the tortuosity of the connected pore space [Blair et al. 1996] and can

sometimes be measured or calculated using a power law

$$F = \phi^{-m}, \tag{2.17}$$

found empirically by Archie [1942]. More about Kozeny-Carman equations follows later (Chapter 4, and Chapter 6).

S_2 is defined for isotropic two-component material by Berryman [1985] as the probability that two points separated by a distance r both lie in the pore space. S_2 is a two-dimensional autocorrelation function [Blair et al., 1996] and both S_1 and S_2 can be defined in terms of the indicator function $f(\mathbf{x})$ described above [Blair et al. 1996]

$$S_1 = \langle f(\mathbf{x}) \rangle = \phi = S_2(0) \tag{2.18}$$

and

$$S_2(r) = \langle f\mathbf{x} \ f(\mathbf{x} + \mathbf{r}) \rangle, \tag{2.19}$$

where the angle brackets denote volume averaging over all positions $\mathbf{x}$, and $r = |\mathbf{r}|$. Berryman [1985] provides a discretized version of Equation (2.19) to compute S_2,

$$S_2(m, n) = \frac{1}{N_2} \sum_{i=1}^{i_{max}} \sum_{j=1}^{j_{max}} f_{ij} f_{i+m, j+n}, \tag{2.20}$$

where $i_{max} = a - m$, $j_{max} = b - n$, a is the image width, b is the image height, $N_2 = i_{max} \times j_{max}$, for distances $r = \sqrt{m^2 + n^2}$ with $0 \leq m \leq a$ and $0 \leq n \leq b$. Figure 2.7 shows two-point correlation functions for fully penetrable (short dashed curve) sphere models (the case of vesicular basalts) and impenetrable (solid curve) ones (granular material) [after Berryman and Blair, 1986].

The slope of the curve of S_2 close to $r = 0$ is

$$S_2'(0) = -\frac{s}{4}, \tag{2.21}$$

[Debye et al., 1957; Berryman and Blair, 1986; Berryman, 1987], where the specific surface area s is defined as the ratio of the pore-grain interface to the total volume
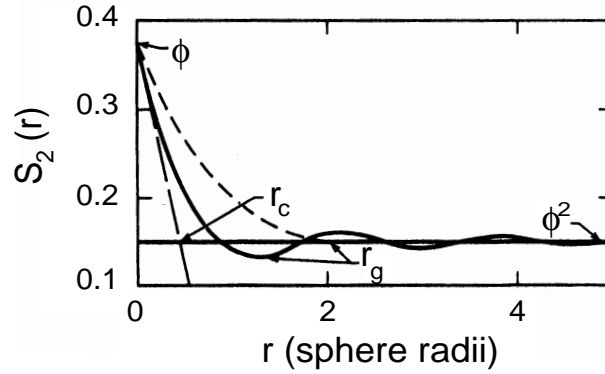
Figure 2.7: Two-point correlation functions for the fully-penetratable (short dashed curve) and the inpenetratable (solid curve) sphere model [from Blair et al., 1996]. The specific surface area s of a material is given by the slope of the line (S_2') as $r \to 0$ in Equation 2.21.

of the porous material. In the equivalent channel model [Paterson, 1983] it can be interpreted as the circumference of the pores divided by the total area of the image. Note that Equation (2.21) is true for any porous material regardless of particle shape [Blair et al., 1996], making it a powerful tool for the determination of specific surface area and therefore potentially for permeability estimation. However, the determination of s by two-point correlation functions assumes that all pores are connected and that the image is representative of the fluid flow determining pathway geometries. The latter condition will be a crucial point later on.

Chapter 3

Measurements and Observations

In this chapter I describe measurements, obtained by the techniques discussed in the previous chapter. After introducing several permeability models in the following chapter, I discuss and interpret these measurements in Chapter 5 and 6.

Table 3.1 provides a summary of measurements, made on the 39 samples. Samples are classified as scoria (cinder cones), flow1, and flow2 samples; measurements include total porosity ϕ_t, porosity determined by image analysis ϕ_{image}, connected porosity ϕ_c, measured permeability k, specific surface area s, characteristic bubble area A_c, bubble roundness R_{round}, and the resolution used for scanning procedures.

Typical measured permeabilities of the basalt samples range from 10^{-17} m^2 to 10^{-10} m^2. Thus the highest measured permeabilities of $k \approx 10^{-10}$ m^2 are comparable with measured permeabilities of very young, unaltered, dike-free Hawaiian lava flows, which show permeabilities of $k \approx 10^{-10}$ m^2 [e.g. Williams et al., 1973; Ingebritsen et al., 1993]. These permeabilities, however, represent the overall horizontal aquifer permeability, including rubble zones, fractures and lava flow layering, which introduces some anisotropy [Ingebritsen et al., 1993]. Therefore the total aquifer permeabilities are expected to be higher than the matrix permeability (see Chapter 1). My measured permeabilities are also in good agreement with Freeze and Cherry [1979, p. 29] who report a permeability of 10^{-14} m$^2 < k < 10^{-9}$ m^2 for vesicular basalts.

Table 3.1: Measurements: total porosity ϕ_t, porosity determined by image analysis ϕ_{ima}, connected porosity ϕ_c, measured permeability k, specific surface area s, characteristic bubble area A_c, bubble roundness R_{rou} and the resolution res, used for scanning procedures.

core	type	ϕ_t	ϕ_{im}	ϕ_c	k	s	A_c	R_{rou}	res
		[%]	[%]	[%]	m^2	1/m	mm		dpi
301	flow2	18.0	17.2	19.5	1.1×10^{-12}	0.612×10^3	4.13	2.02	1000
302	flow2	16.9	18.2	17.6	1.2×10^{-14}	0.705×10^3	7.15	2.26	800
303	flow2	18.1	28.1	19.9	2.6×10^{-13}	0.836×10^3	9.77	2.01	900
304	flow2	18.5	22.7	21.5	6.3×10^{-13}	0.835×10^3	6.86	2.02	800
30101	flow2	17.8	17.2	19.6	1.2×10^{-13}	0.612×10^3	4.13	2.02	1000
30102	flow2	18.2	17.2	19.5	3.9×10^{-12}	0.612×10^3	4.13	2.02	1000
30103	flow2	16.4	17.2	19.5	3.3×10^{-13}	0.612×10^3	4.13	2.02	1000
402	flow2	10.5	14.3	16.0	1.6×10^{-13}	1.18×10^3	1.28	1.92	1200
501	scoria	46.4	45.5	47.8	1.4×10^{-13}	2.66×10^3	3.50	1.83	1100
50101	scoria	48.8	45.5	47.8	2.0×10^{-13}	2.66×10^3	3.50	1.83	1100
50102	scoria	44.2	45.5	47.8	9.1×10^{-14}	2.66×10^3	3.50	1.83	1100
601	flow1	47.2	52.0	46.6	5.1×10^{-12}	2.44×10^3	3.63	1.63	1100
701	flow1	49.8	40.6	49.1	2.3×10^{-13}	2.30×10^3	7.41	1.53	800
1001	flow2	19.4	16.9	21.1	5.3×10^{-12}	1.71×10^3	0.98	2.07	1200
1301	flow2	14.3	18.1	10.2	1.0×10^{-13}	0.689×10^3	6.74	2.28	800
1401	flow2	26.3	29.5	27.0	3.3×10^{-13}	0.923×10^3	9.14	1.92	700
1402	flow2	23.2	27.6	25.4	1.1×10^{-12}	0.868×10^3	7.83	1.96	800
1404	flow2	23.1	33.1	23.8	1.7×10^{-12}	0.876×10^3	9.46	1.96	700
1601	flow1	41.0	38.4	44.4	9.3×10^{-13}	1.26×10^3	19.2	1.81	600
1602	flow1	38.9	44.3	44.7	2.1×10^{-12}	1.31×10^3	32.5	1.73	400
1902	flow2	22.5	32.6	25.3	1.4×10^{-11}	0.931×10^3	7.06	1.96	800
2001	scoria	75.4	69.8	78.9	9.4×10^{-12}	1.44×10^3	47.6	1.59	400
21012	flow1	42.8	45.8	45.3	7.6×10^{-13}	0.889×10^3	7.63	1.64	800
2102	flow1	35.2	34.0	34.7	1.0×10^{-14}	0.876×10^3	7.63	1.64	700
2201	flow1	45.9	40.3	46.6	3.7×10^{-12}	0.758×10^3	18.6	1.76	500
2301	scoria	66.6	63.0	69.0	1.4×10^{-11}	1.96×10^3	22.8	1.62	600

Table 3.1:

Table 3.1: (Continued)

core	type	ϕ_t	ϕ_{im}	ϕ_c	k	s	A_c	R_{rou}	res
		[%]	[%]	[%]	m^2	1/m	mm		dpi
2401	scoria	67.0	64.0	70.4	2.8×10^{-12}	2.25×10^3	11.5	1.68	700
2501	flow1	35.3	34.2	36.7	1.0×10^{-13}	3.88×10^3	0.51	1.51	1200
2502	flow1	36.5	34.2	42.1	2.4×10^{-13}	3.88×10^3	0.51	1.51	1200
2601	scoria	66.0	62.9	70.2	5.2×10^{-12}	3.27×10^3	13.0	1.87	600
2801	scoria	53.6	54.5	57.4	1.5×10^{-12}	2.30×10^3	6.03	1.61	900
2802	scoria	55.7	54.5	60.4	7.6×10^{-13}	2.30×10^3	6.14	1.61	900
2803	scoria	56.8	64.4	58.4	9.1×10^{-13}	1.40×10^3	14.8	1.55	600
3101	flow1	41.5	30.9	43.0	2.9×10^{-12}	0.843×10^3	11.0	1.63	700
3201	flow1	45.4	40.9	46.5	2.0×10^{-13}	0.614×10^3	23.4	1.63	500
320101	flow1	43.2	40.9	44.6	2.0×10^{-13}	0.614×10^3	23.4	1.63	500
320102	flow1	46.7	40.9	48.3	2.4×10^{-13}	0.614×10^3	23.4	1.63	500
3301	flow1	46.4	41.2	47.0	1.6×10^{-13}	0.846×10^3	20.6	1.63	600
330101	flow1	46.3	41.2	47.1	4.0×10^{-13}	0.846×10^3	20.6	1.63	600

The total macroporosity ranges from 10 to 80%. Microporosity is not included in this value, although it can be observed in thin sections of some basalt flow samples (Figure 3.4). Samples having 0 % macroporosity still show microporosity and related permeabilities on the order of 10^{-17} m^2. This "micropermeability" is probably due to intercrystalline micropores. In the following I am addressing how the abundance, structure and shape of macropores governs the permeability. Therefore the porosity due to micropores and the resulting "micropermeability" are neglected and assumed to be zero when no macropores are abundant.

A plot of total porosity versus permeability for all samples shows a diagonal lower bound, a variability of k over three orders of magnitude for a given porosity ϕ and a strong dependence of permeability on the abundance of macropores (Figure 3.1). A total of 62 samples were examined, but 20 samples show signs of weathering and secondary mineralization (Diamond Crater and Cow Lake samples) or fractures and 3 samples do not contain macropores (see Figure 3.1).
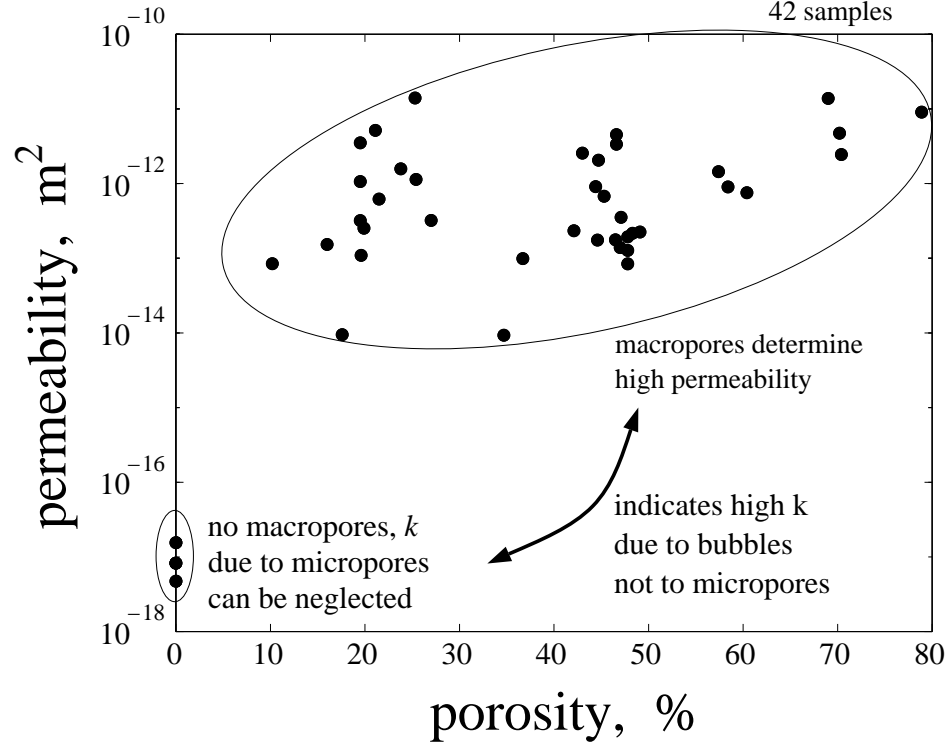
42 samples

no macropores, k
due to micropores
can be neglected

macropores determine
high permeability

indicates high k
due to bubbles
not to micropores

Figure 3.1: ϕ-k relationship (not normalized, all samples). ϕ-k relationship of the 42 basalt samples. A diagonal lower bound on permeability can be observed. Typical permeability values are in the range 10^{-17} m^2 $< k < 10^{-11}$ m^2. The variability of k for a given porosity ϕ is about three orders of magnitude. No distinct ϕ-k relationship can be observed, because no microstructural parameters are taken into account. The three samples with a distinctively lower permeability of $k \approx 10^{-17}$ m^2 and a porosity of $\phi \approx 0\%$ show no macropores. This indicates that the high permeabilities for vesicular basalts are governed bu the macropores. Porosity and permeability due to micropores are neglected hereafter.

As is commonly observed, permeability values vary over a range of about 4 orders of magnitude for a given porosity. For comparisson Blair et al. [1996] observe over 3 orders of magnitude variation of k within a narrow porosity range of a few percent in the same sandstone. In general, it is expected that the permeability range increases with increasing heterogeneity of the sample [Blair et al., 1996].

The samples used here were taken from two different rock types, basaltic andesite flows and cinder cones. Because these reflect different emplacement mechanisms, they are therefore distinguished in the following discussion.

In the Oregon Cascades one can observe lava flows and cinder cones next to, and on top of, each other. This indicates the possible change of one type of eruption into the other (e.g. Lava Butte Cinder Cone and Lava Butte flow). This is currently observed on Hawaii (e.g. Wolfe et al., 1989). The emplacement mechanism probably depends on lava extrusion velocity which in turn is a function of vent geometry, lava flux, and magma chamber dynamics causing pressure variations.

The scoria of the cinder cones is formed during high velocity fountain eruptions [Mangan and Cashman, 1996] and usually chilled rapidly, mostly while it is still in the air, forming a glassy rock matrix (see Figure 3.2). The low viscosity, $\mu \approx 10^2$ PaS, of the basaltic lava [Bottinga et al., 1972], high surface tension of the basalt-air interface, $\sigma \approx 0.35$ N/m [Khitarov et al., 1979; Walker et al., 1981], and the small vesicle radii of $r \approx 1$ mm, lead to low capillary numbers Ca. Assuming a bubble deformation from an aspect ratio of 1 to 2 (strain $= 1$) within 10 seconds yields a strain rate of $\epsilon = 10^{-1}$ s^{-1}. The capillary number is therefore on the order of

$$Ca = \frac{r\mu\epsilon}{\sigma} \approx \frac{1}{30}. \tag{3.1}$$

The distortion of a sphere to an ellipsoid is linearly proportional to Ca for low Ca, and proportional to Ca^3 for high capillary numbers [Taylor, 1932]. The Capillary number
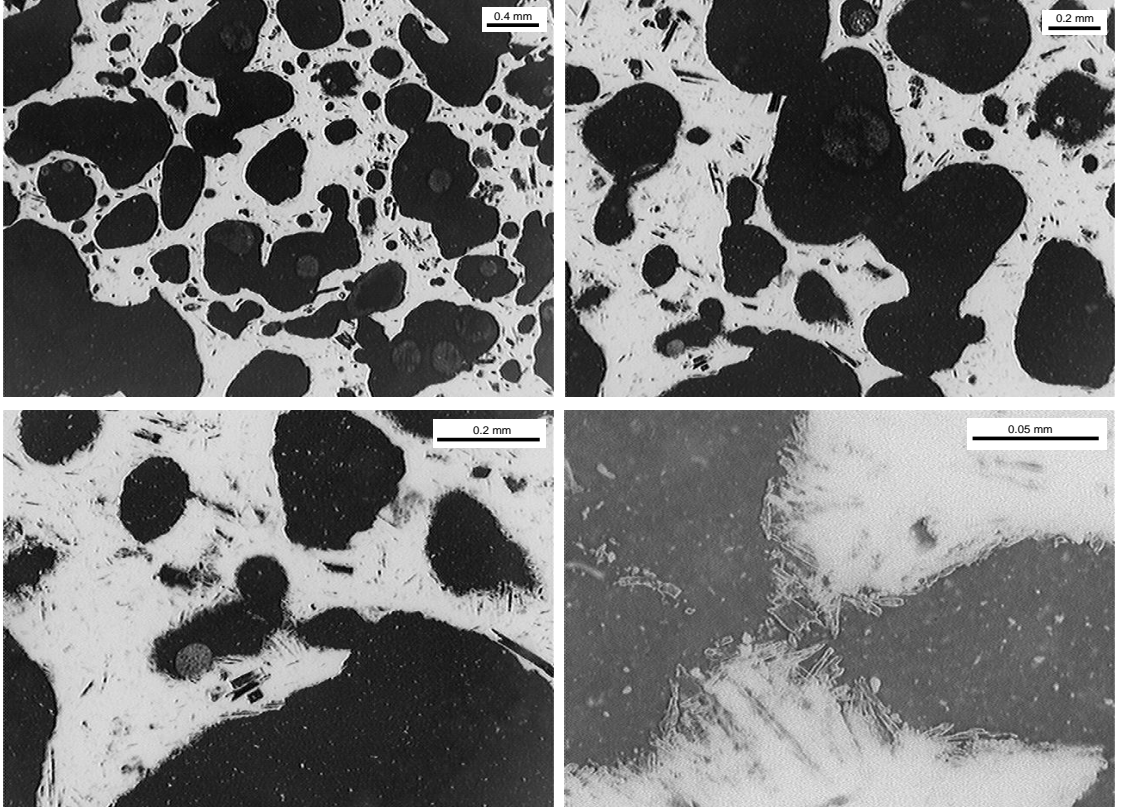
Figure 3.2: Thin section image of a scoria sample. Various magnifications of a thin section image of a scoria sample (b020-2,3) showing connected, but not collapsed bubbles. The interbubble aperture is much smaller than the bubbles themselves. black: bubbles and crystals (mostly feldspar), white: glassy rock matrix.

characterizes the relative importance of viscous stresses compared to surface tension stresses. Because $Ca \ll 1$, surface tension dominates and bubbles remain subspherical (Figure 3.2) despite high bubble connectivity (Figure 2.5). Rapid quenching of the lava allows the preservation of the subspherical shape because relaxation of the thin film in between bubbles is impeded. Interbubble aperture sizes therefore remain small. Reaching the ground, the already quenched lava cannot deform in a ductile style but breaks brittly into pieces of scoria of various sizes. Some breakup might occur in the air as well.

In contrast to cinder cone samples, the flow samples are produced by lower velocity eruptions, where the lava is not dispersed in the air but forms relatively thick flows. The top and, to a lesser degree, the bottom of the flows cool and insulate the middle parts of the flow [e.g. Lipman et al., 1987; Crisp et al., 1994]. This leads to slower cooling rates allowing ductile deformation of the rock matrix and the bubbles as a result of shear flow.

The slow cooling rate of the flows allows considerable deformation to occur. The accumulated deformation results in increasing bubble elongation with increasing distance from the vent accompanied by an increase in crystallinity. Although this is a continuous process, I divide the flow samples in two distinct categories, based on their microstructure.

The first category called "flow1" samples (Figure 3.3), represents samples that probably cooled relatively close to the vent and therefore show a predominantly glassy matrix surrounding ellipsoidal bubbles. The bubbles are elongated in flow direction. Flow1 samples contain few or no micropores since intercrystalline space is mostly filled with glass.

The second category called "flow2" samples (Figure 3.4) represents samples that were collected further away from the vent, and show a large degree of vesicle elongation and sometimes a diktytaxitic texture. The slow cooling rates of flow2 samples, indicated by large crystals abundances, allow relaxation of the thin film between bubbles. The drainage of the film increases the permeability, allows degassing, and leads to bubble collapse perpendicular to bubble elongations.

Roundness calculations were performed using Equation (2.16). Scoria and flow1 bubbles are systematically rounder than flow2 bubbles (Figure 3.5) reflecting bubble collapse in flow2 samples. Table 3.2 is a summary of the three vesicular basalt types and the main characteristics important for later discussions. Figure 3.6 shows the
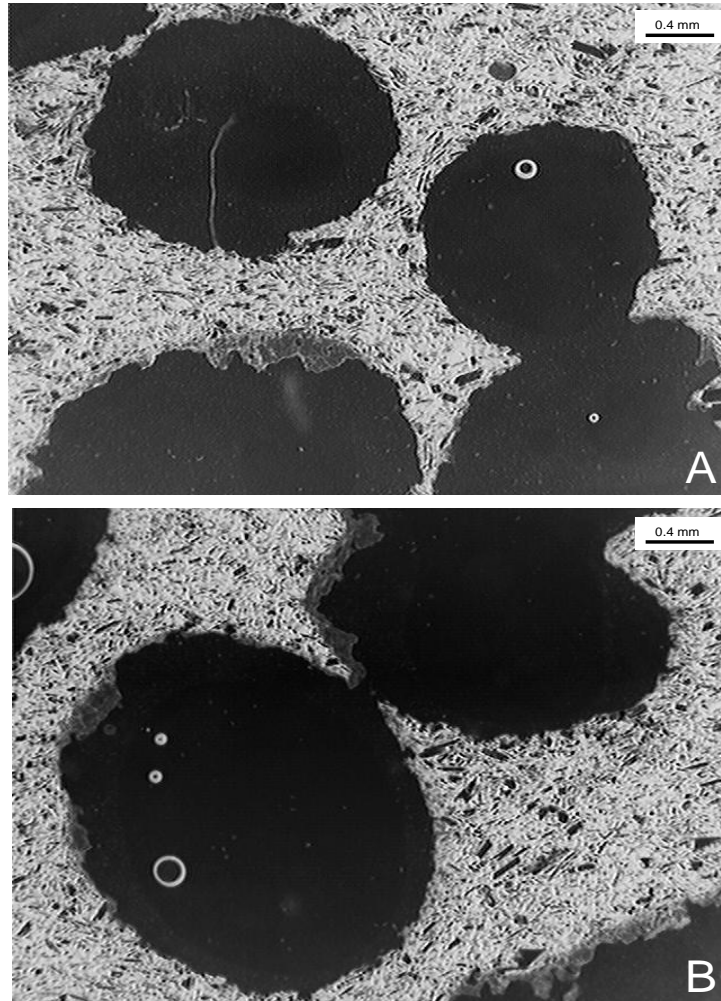
Figure 3.3: Thin section image of a flow1 sample (b021-02) showing connected, but not collapsed bubbles. The interbubble aperture is relatively narrow in many cases (B), but shows signs of widening (A) due to slower cooling rates and film drainage. This allows enhanced permeability (see text). Micropores are largely absent. Black: bubbles and crystals (mostly feldspar). White: glassy rock matrix.
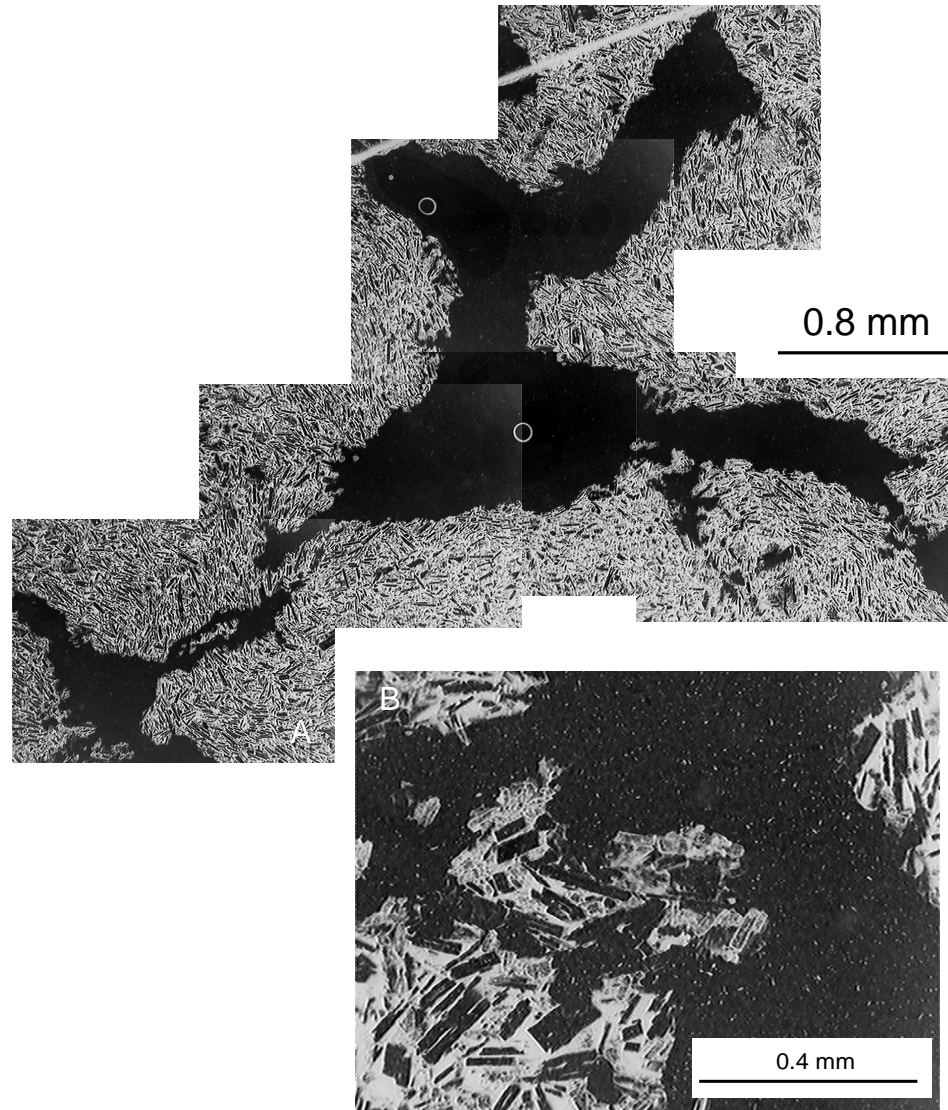
Figure 3.4: Thin section image of a flow2 sample. Assemblage of thin section images of a flow2 sample (b013-01) showing extremely well-connected, and collapsed bubbles. The interbubble aperture is not much smaller than the bubbles themselves. Micropores indicate a diktytaxitic texture. Some connections appear to be collapsed. Black: bubbles and crystals (mostly feldspar). White: glassy rock matrix.
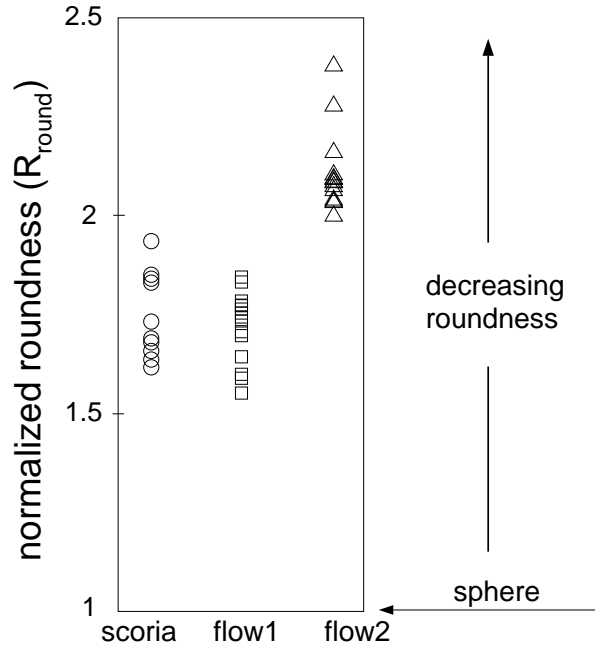
Figure 3.5: Roundness values (R_{round}) for scoria and basalt flow bubbles. $R_{\text{round}} = 1$ indicates a perfect sphere. Higher values indicate decreasing roundness. Scoria and flow1 samples show relatively low R_{round} values indicating high bubble roundnesses. In contrast bubbles in flow2 samples are less round which is indicated by higher R_{round} values.

Table 3.2: Characteristics of the three basalt sample types

	bubble shape	matrix texture	formation	symbol
scoria	subspherical not collapsed	glassy no micropores	fountain eruption (cinder cone)	filled circles
flow1	ellipsoidal not collapsed	glassy no micropores	close to the vent	open squares
flow2	elongated collapsed	∼ holocrystalline micropores, dyktitaxitic	distal from vent	filled triangles

Table 3.2:

34

same data as Figure 3.1, but subdivided into those three categories. One can see that the scoria samples plot approximately on a curve showing increasing permeability for increasing porosity whereas the flow samples lack such a ϕ-k relation. This increase in k for an increase in ϕ was also noticed in pumice that was not highly deformed (Katharine Cashman, pers. com, 1998). Some models and ideas are introduced in the following Chapter in order to gain more information about ϕ-k relation and about the influence of porosity, microstructure and average bubble sizes. Interpretation of the measurements and observations in this Chapter follow then in Chapter 5. Chapter 6 discusses the possibility of calculating the permeability of vesicular materials using Kozeny-Carman equations and image analysis techniques.
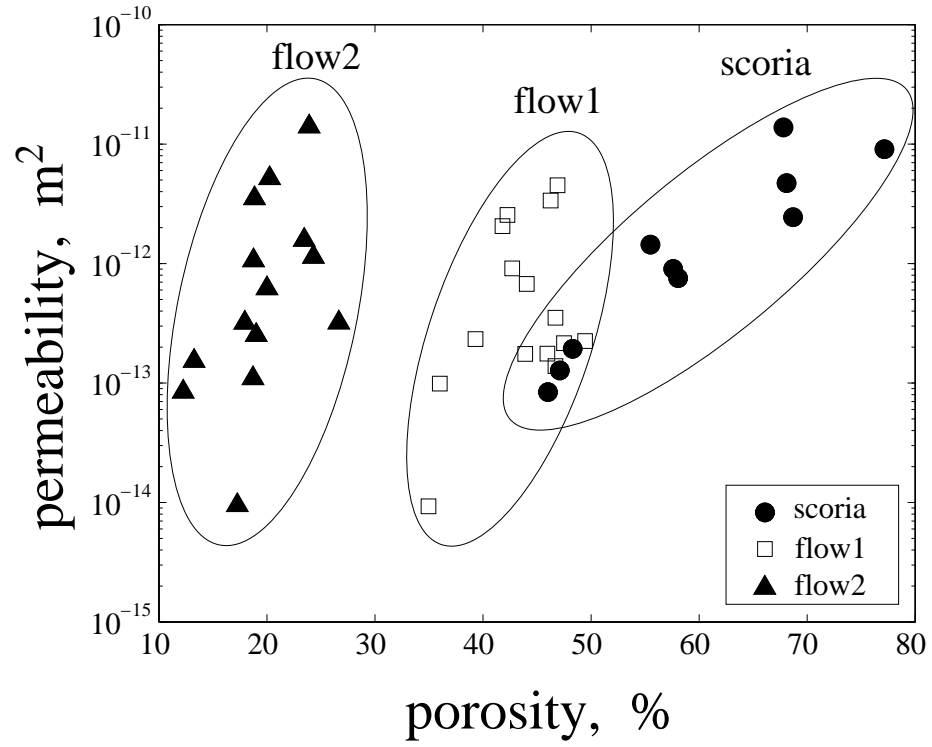
Figure 3.6: ϕ-k relationship for scoria, flow1 and flow2 samples. Three distinct clusters representing the three different microstructural characteristics of scoria (filled circles), flow1 (open squares) and flow2 (filled triangles) samples can be observed. This indicates a pronounced dependence of a ϕ-k relationship on the microstructure of the material investigated.

Chapter 4

Permeability Models

This chapter deals with models that can be used to estimate permeability. Such models also provide a basis for interpreting the permeability measurements of Chapter 3 and to gain an understanding of the relationship between a material's microstructure and its permeability. Actual interpretations of measurements are provided in Chapter 5 using the percolation theory introduced in this chapter. Chapter 6 then deals with permeability estimates, based on the Image-Analysis-Kozeny-Carman model also introduced in this chapter.

As mentioned in the introduction, there exists a long history of modeling a porosity permeability relations that goes back to Rose [1945] who proposed that

$$k \sim \phi^m, \tag{4.1}$$

where m is an exponent that is typically determined empirically. This power law relationship is similar to Archie's law, Equation (4.8), and percolation theory models which will be discussed in section 4. However, early on it was recognized that there is no simple relationship between porosity and permeability [Cloud, 1941]. Microstructural parameters, accounting for pore space connectivity and pathway tortuosity, have to be taken into account as well. Sahimi [1995, p. 6] notes that the continuum models used here are not well-suited when interconnectiveness of pores play a major

role. However, these models are simpler to apply as they do not require the large computations necessary for discrete models which would be more appropriate when pore space connectiveness is important. Figure 2.5, however, shows that virtually all pores in cinder cones as well as in basalt flows are connected justifying the use of a continuum model.

Since the work of Kozeny and Carman [Carman, 1956; Dullien, 1979] there have been numerous reasonably successful attempts to find a model that can estimate the fluid permeability for a porous material when microstructural information is available. Roberts et al. [1997] provide a recent comparison of laboratory, analytical, and imaging techniques for estimating permeability in porous media. Blair et al. [1996] compare the Katz-Thompson [1986] approach invoking a combination of percolation theory concepts [Stauffer, 1985; Sahimi, 1994] with mercury injection porosimetry with the Λ-parameter method of Johnson et al. [1986] and their own image processing method that is used to obtain values for Kozeny-Carman equations. Percolation theory can also be used in power law relations to estimate fluid permeability [Sahimi, 1994, 1995]. The two approaches followed in this thesis are the percolation theory method and the image-analysis-Kozeny-Carman-equation method introduced by Berryman et al. [1987] and Blair et al. [1996].

4.1   Katz & Thompson Model

Katz and Thompson [1986] use a formula for estimating permeability that can be written as

$$k = \frac{l_c^2}{226F} \tag{4.2}$$

where l_c is a critical pore diameter that indicates the smallest of the largest pores that are assumed to contribute to the percolation network. Pores smaller than l_c are assumed to conduct a significantly smaller volume of fluid and can therefore be

neglected. F is the formation factor determined by electrical conductivity measurements (ratio of the pore fluid conductivity, σ_o, to the effective conductivity of a porous material saturated with that fluid, σ, i.e., $F = \sigma_o/\sigma$). The constant $1/226$ is a theoretical value that, among other things, depends on the pore geometry. The characteristic length l_c is determined by the mercury porosimetry injection method[1]. In Equation (4.2) permeability is directly proportional to the characteristic length scale squared and inversely proportional to the formation factor.

4.2   Johnson Model

Johnson et al. [1986] introduce a characteristic length Λ that can be determined by electrical conductivity measurements of porous materials. Λ is given by

$$\Lambda \equiv 2\frac{\int_V |\mathbf{E}|^2 dV}{\int_S |\mathbf{E}|^2 ds}, \tag{4.3}$$

where $\mathbf{E}$ is the local electrical field, V the pore volume and s the surface area. If the pores are smooth, for example cylindrical tubes, then the local electrical field is constant and Equation (4.3) reduces to $\Lambda = 1/s = l_c$, where s is the specific surface area (surface area per unit volume). If the pore geometry is highly variable, the local electrical field $\mathbf{E}$ varies and the regions with the highest $\mathbf{E}$ will have the biggest impact on both Λ and the fluid permeability and electrical conductivity. The permeability is determined by:

$$k = \frac{\Lambda^2}{8F} = \frac{l_c^2}{8F}. \tag{4.4}$$

Again the permeability is directly proportional to the characteristic length l_c squared and inversely proportional to the formation factor F.

---

[1] I don't use this method, because it is too unhealthy.

4.3 Image-Analysis-Kozeny-Carman (IAKC) Model

The image analysis method by Berryman et al. [1987] and Blair et al. [1996] used in combination with Kozeny-Carman equations [Carman, 1956; Dullien, 1979] is the method I use in this thesis. It has one signifcant advantage advantage over the other methods introduced above, namely that permeabilities can be estimated from images of the rock texture. In addition, measurements are inexpensive and can be quickly made because they can be done with standard Personal Computers. The general form of a Kozeny-Carman relation is

$$k = \frac{\phi r^2}{c},$$
(4.5)

where k is the permeability, ϕ the porosity, r the hydraulic radius and c a constant reflecting the pore geometry. For circular tubes, $c = 2$, and for flat cracks, $c = 3$ [Berryman et al., 1987]. Paterson [1983] and Walsh and Brace [1984] introduced a form of the Kozeny-Carman relation that reflects flow in a porous medium by an arrangement of parallel cylindrical pores called the equivalent channel model:

$$k = \frac{\phi^2}{cFs^2},$$
(4.6)

where s is the specific surface area, F the formation factor, $c = 2$ for circular tubes and ϕ again the porosity. Although the equivalent channel model is a geometrical simplification of a more complex real rock, it may in some cases be appropriate for vesicular basalt flow samples where vesicles are ellipsoids elongated in flow direction and thus approach a cylindrical shape. For this to hold true, however, the bubbles must be connected. This constraint turns out to be crucial for permeability estimations in vesicular materials and is discussed in Chapter 6. It is therefore necessary to carry out image analysis on cross sections perpendicular to the averaged longest

axis of the ellipsoids. When cores are drilled from small boulders I choose the long axis of the core to be as parallel as possible to the average elongation direction of the bubbles in order to satisfy the above mentioned condition. The characteristic length for Equation (4.6) can be defined by $l = \phi/s$, so that (4.6) can be written as

$$k = \frac{l^2}{cF},\qquad(4.7)$$

where the formation factor F can be measured (electrical conductivity, mercury injection porosimetry) or can be estimated using the empirical law found by Archie [1942]

$$F = \Phi^{-m}.\qquad(4.8)$$

The exponent m is subject to discussion, but has been estimated by Archie [1942] to be between 1.8 and 2 for consolidated sandstones and by Brace [1977] and Wong et al. [1984] to be about 2 for rocks. Values of m should be 1.5 for an isotropic medium containing spherical particles (impermeable spheres) and increase ($m > 1.5$) for nonspherical particles [Archie, 1942; Sen et al., 1981]. In the calculations presented here I use either a constant exponent of $m = 2$ in Equation (4.8) or an exponent increasing from 1.5 to higher values with decreasing bubble roundness.

As noted by Blair et al. [1996], it is obvious that in Equations (4.7), (4.4) and (4.2), the permeability is directly proportional to the characteristic length squared and inversely proportional to the formation factor. Blair et al. [1996] further expect that the characteristic length is the same in all three methods, since there can be only one pertinent characteristic length in the permeability estimation problem for homogeneous material.

When determining the specific surface area s using two point correlation functions it is crucial to use the right image magnification [Berryman et al., 1987]. Berryman et al. [1987] point out that image processing techniques do not measure the true

specific surface area of the investigated material, but instead smooth the walls of pores because of the necessary image discretization. Specific surface areas obtained by this method underestimate more realistic surface area measurements using gas absorption techniques. However they note that the Kozeny-Carman relation is itself only an approximation, representing smooth-walled cylinders and approximations of tortuosity. Therefore they state that it is exactly this smooth wall approximation provided by image analysis that is appropriate to use as the specific surface area in Kozeny-Carman equations. Further they suggest that the correct magnification is achieved when a typical correlation length (radius of an average bubble) comprises approximately 100 pixels (discrete picture elements). This ensures that the pore radius is measured to an accuracy of 1 % which leads to a maximum permeability estimation error of 4 % [Berryman et al., 1987].

Magnifications have to be chosen carefully, especially if correlation functions are determined for granular material, because fluids flow around impermeable spheres and pores are thin necks. The size of these necks can easily be under- or over-estimated by improper magnifications. Too high magnifications lead to overestimations of the specific surface area with respect to their use in Kozeny-Carman equations [Berryman et al., 1987] and therefore to underestimations of the permeability. In the case of vesicular basalts, however, the pores have an ellipsoidal shape which is not as sensitive to size measurement errors due to magnification. This can be observed in Figure 4.1a, which shows calculated specific surface areas s for different magnifications (resolution from 100 to 1200 dpi) of the exact same image. Magnification is expressed in pixels per characteristic bubble cross sectional radius. The calculated specific surface area stays approximately constant for resolutions (magnifications) larger than a resolution of 40 pixels per characteristic bubble radius. Specific surface areas determined by resolutions significantly below 40 pixels per characteristic bubble radius are too small

(Figure 4.1a).

This result differs from the measurements Berryman at al. [1987] made for Berea sandstone where the specific surface area increases constantly for increasing, low magnifications (Figure 4.1b). The highest magnification shown in Figure 4.1b provides an estimate of the smoothed image specific surface [Berryman et al., 1987].

My result of approximately constant specific surface area for vesicular basalt at different resolutions ($>$ 40 pixels per bubble radius) is used in the following as a verification for the choice of resolution for the individual samples. It is not necessary to increase the resolution above the critical resolution for a given sample which helps to reduce calculation times. The characteristic bubble radius r_c was determined using the characteristic bubble area A_c, assuming a circular shape so that $A_c = \pi r_c^2$. r_c then can be used to determine the critical resolution (in dpi) to which 100 dpi were added and then rounded to the next higher hundred-value (see Table 4.1). The actual fluid flow through penetratable overlapping spheres is mainly determined by the narrow aperture sizes of the overlapping spheres. Therefore specific surface area should ideally be measured on those aperture sizes exclusively and not averaged over the complete bubble network.

Two point correlation functions are very sensitive to an anisotropy shown by the analyzed images. Figure 4.1 shows the specific surface area for one image (Figure 4.2) of a specific sample (b032-01) determined by:

- choosing second point in x-direction only
- choosing second point in y-direction only
- choosing second point for various x and y directions

It can be observed that the image has an anisotropy expressed by a slight bubble elongation in the y-direction (Figure 4.2), which results in smaller specific surface
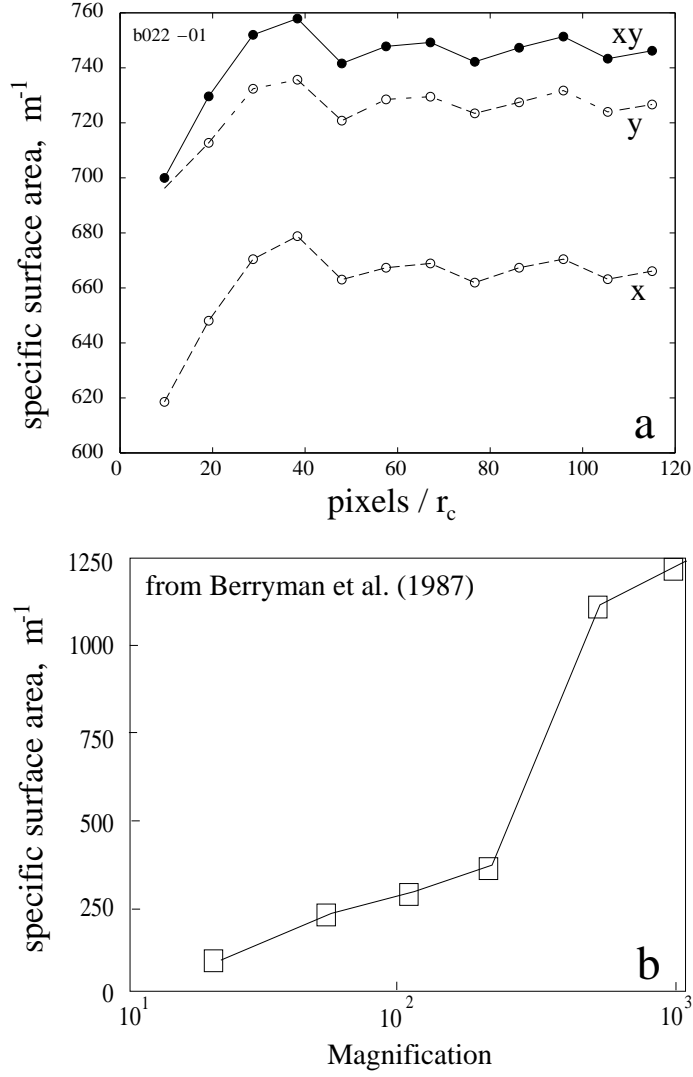
Figure 4.1: Resolution effect on specific surface area s in (a) vesicular materials and in (b) granular materials, determined by two-point correlation functions. In vesicular materials the determined specific surface area stays approximately constant for resolutions greater than 40 pixel per characteristic bubble radius. Two-point correlation function calculated in xy-direction combined (solid line), x-direction only (dashed line) and y-direction only (dotted line) (see also Figure 4.2). By contrast, in granular materials (b, from Berryman et al. 1987) a continuous increase in specific surface area can be observed.
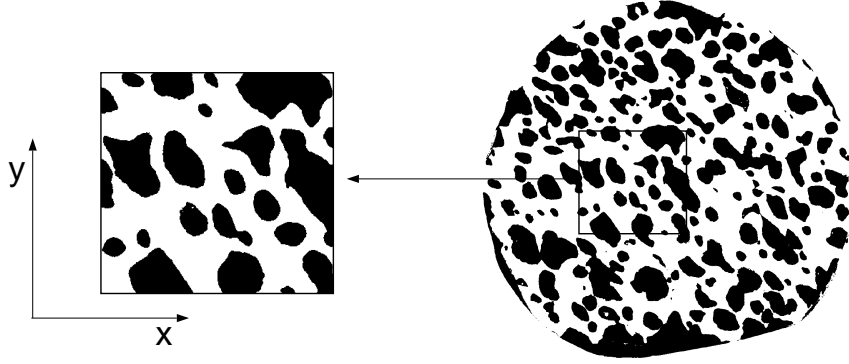
Figure 4.2: Image used for Figure 4.1a

values for calculations in this direction.

This anisotropy is due to the fact that it is not always possible to drill the cores exactly parallel to bubble elongations. Bubbles in shear flows also do not have circular cross sections [e.g. Kennedy et al., 1993]. These bubbles may have elliptical cross sections which will show up as specific surface area anisotropy, as discussed above. I accounted for this effect by calculating the two-point correlation function by varying directions between the two points as combinations of x and y (solid line in Figure 4.1a).

The basalt samples were scanned at resolutions varying from 500 to 1200 dpi depending on A_c. This resolution is sufficient for most of the samples, because they show relatively large average vesicle sizes. Nine samples, however, contain very small vesicles for which a higher scanning resolution (up to over 4000 dpi) than 1200 dpi would have been desirable, but is not available to me at this point. A larger error in permeability calculations has to be expected for those samples. Lower resolutions are likely to underestimate the specific surface area and therefore overestimate the permeability of a medium. A solution to this problem could be to use thin sections instead of cores for the image analysis. Images obtained from thin sections using crossed polarizers have to be thresholded in an image processing program in order to

obtain a pure black and white image. This procedure, however, is more subjective than the bitmap scanning process since a threshold value has to be chosen to separate vesicles from rock matrix in the image.

For each sample, I determined porosity using S_1, Equation (2.18), and specific surface area s using Equation (2.21), where S_2 was determined by Equation (2.19) in its discretized form, Equation (2.20). I calculated expected permeabilities by using formation factors determined by Equation (4.8) and compared these with measured values and with percolation theory models (see Chapter 6).

Table 4.1 provides the data used to calculate permeability, using the IAKC model. The obtained permeability values are listed as well as the measured permeabilities for comparisson.

4.4   Percolation Theory: The Fully Penetratable Sphere Model

Percolation theory ideas can also be used to estimate permeabilities for given porosities. An introduction to percolation theory is provided by Stauffer [1985], general applications are described by Sahimi [1994], and applications of percolation theory to flow in porous media are presented in Sahimi [1995]. In the following I will concentrate on the aspects of percolation theory related to fluid percolation through a porous medium, a process that is in some ways similar to electrical conduction in a network of conductors. This analogy leads to the development of permeability estimation methods involving among other parameters (porosity, tortuosity, pore space connectedness) the measurement of electrical conductivity of a porous nonconducting material that is filled with a conducting fluid [Katz et al., 1986]. However a porosity-permeability power law relation can be investigated even if no microstruc-

46

Table 4.1: Calculated and measured permeability and input data: total porosity (ϕ_t), connected porosity (ϕ_c), specific surface area (s), resolution (res), used for scanning procedures, formation factor F, measured permeability (k_m) and calculated permeability k_c.

core	type	ϕ_t	ϕ_c	s	res	F	k_m	k_c
		[%]	[%]	1/m	dpi		m^2	m^2
301	flow2	18.0	19.5	0.612 $\times 10^3$	1000	28.4	1.1 $\times 10^{-12}$	1.6 $\times 10^{-09}$
302	flow2	16.9	17.6	0.705 $\times 10^3$	800	33.6	1.2 $\times 10^{-14}$	8.9 $\times 10^{-10}$
303	flow2	18.1	19.9	0.836 $\times 10^3$	900	27.7	2.6 $\times 10^{-13}$	9.3 $\times 10^{-10}$
304	flow2	18.5	21.5	0.835 $\times 10^3$	800	25.0	6.3 $\times 10^{-13}$	1.1 $\times 10^{-09}$
30101	flow2	17.8	19.6	0.612 $\times 10^3$	1000	28.6	1.2 $\times 10^{-13}$	1.6 $\times 10^{-09}$
30102	flow2	18.2	19.5	0.612 $\times 10^3$	1000	28.1	3.9 $\times 10^{-12}$	1.7 $\times 10^{-09}$
30103	flow2	16.4	19.5	0.612 $\times 10^3$	1000	31.0	3.3 $\times 10^{-13}$	1.4 $\times 10^{-09}$
402	flow2	10.5	16.0	1.18 $\times 10^3$	1200	57.0	1.6 $\times 10^{-13}$	1.1 $\times 10^{-10}$
501	scoria	46.4	47.8	2.66 $\times 10^3$	1100	4.50	1.4 $\times 10^{-13}$	3.5 $\times 10^{-09}$
50101	scoria	48.8	47.8	2.66 $\times 10^3$	1100	4.28	2.0 $\times 10^{-13}$	3.8 $\times 10^{-09}$
50102	scoria	44.2	47.8	2.66 $\times 10^3$	1100	4.73	9.1 $\times 10^{-14}$	3.2 $\times 10^{-09}$
601	flow1	47.2	46.6	2.45 $\times 10^3$	1100	4.55	5.1 $\times 10^{-12}$	4.0 $\times 10^{-09}$
701	flow1	49.8	49.1	2.30 $\times 10^3$	800	4.09	2.3 $\times 10^{-13}$	5.7 $\times 10^{-09}$
1001	flow2	19.4	21.1	1.71 $\times 10^3$	1200	24.4	5.3 $\times 10^{-12}$	2.9 $\times 10^{-10}$
1301	flow2	14.3	10.2	0.689 $\times 10^3$	800	66.6	1.0 $\times 10^{-13}$	2.4 $\times 10^{-10}$
1401	flow2	26.3	27.0	0.923 $\times 10^3$	700	14.1	3.3 $\times 10^{-13}$	3.0 $\times 10^{-09}$
1402	flow2	23.2	25.4	0.868 $\times 10^3$	800	16.9	1.1 $\times 10^{-12}$	2.3 $\times 10^{-09}$
1404	flow2	23.1	23.8	0.876 $\times 10^3$	700	18.2	1.7 $\times 10^{-12}$	2.0 $\times 10^{-09}$
1601	flow1	41.0	44.4	1.26 $\times 10^3$	600	5.49	9.3 $\times 10^{-13}$	1.1 $\times 10^{-08}$
1602	flow1	38.9	44.7	1.31 $\times 10^3$	400	5.72	2.1 $\times 10^{-12}$	8.9 $\times 10^{-09}$
1902	flow2	22.5	25.3	0.931 $\times 10^3$	800	17.5	1.4 $\times 10^{-11}$	1.9 $\times 10^{-09}$
2001	scoria	75.4	78.9	1.44 $\times 10^3$	400	1.68	9.4 $\times 10^{-12}$	8.6 $\times 10^{-08}$
21012	flow1	42.8	45.3	0.889 $\times 10^3$	800	5.15	7.6 $\times 10^{-13}$	2.4 $\times 10^{-08}$
2102	flow1	35.2	34.7	0.876 $\times 10^3$	700	8.19	1.0 $\times 10^{-14}$	9.7 $\times 10^{-09}$
2201	flow1	45.9	46.6	0.758 $\times 10^3$	500	4.68	3.7 $\times 10^{-12}$	4.0 $\times 10^{-08}$
2301	scoria	66.6	69.0	1.96 $\times 10^3$	600	2.18	1.4 $\times 10^{-11}$	2.7 $\times 10^{-08}$

Table 4.1:

Table 4.1: (Continued)

core	type	ϕ_t	ϕ_c	s	res	F	k_m	k_c
		[%]	[%]	1/m	dpi		m^2	m^2
2401	scoria	67.0	70.4	2.25 $\times 10^3$	700	2.12	2.8 $\times 10^{-12}$	2.2 $\times 10^{-08}$
2501	flow1	35.3	36.7	3.88 $\times 10^3$	1200	7.72	1.0 $\times 10^{-13}$	5.6 $\times 10^{-10}$
2502	flow1	36.5	42.1	3.88 $\times 10^3$	1200	6.48	2.4 $\times 10^{-13}$	7.9 $\times 10^{-10}$
2601	scoria	66.0	70.2	3.27 $\times 10^3$	600	2.16	5.2 $\times 10^{-12}$	1.0 $\times 10^{-08}$
2801	scoria	53.6	57.4	2.29 $\times 10^3$	900	3.25	1.5 $\times 10^{-12}$	9.0 $\times 10^{-09}$
2802	scoria	55.7	60.4	2.29 $\times 10^3$	900	2.97	7.6 $\times 10^{-13}$	1.1 $\times 10^{-08}$
2803	scoria	56.8	58.4	1.39 $\times 10^3$	600	3.01	9.1 $\times 10^{-13}$	2.8 $\times 10^{-08}$
3101	flow1	41.5	43.0	0.843 $\times 10^3$	700	5.60	2.9 $\times 10^{-12}$	2.2 $\times 10^{-08}$
3201	flow1	45.4	46.5	0.614 $\times 10^3$	500	4.74	2.0 $\times 10^{-13}$	5.9 $\times 10^{-08}$
320101	flow1	43.2	44.6	0.614 $\times 10^3$	500	5.19	2.0 $\times 10^{-13}$	4.9 $\times 10^{-08}$
320102	flow1	46.7	48.3	0.614 $\times 10^3$	500	4.43	2.4 $\times 10^{-13}$	6.8 $\times 10^{-08}$
3301	flow1	46.4	47.0	0.846 $\times 10^3$	600	4.59	1.6 $\times 10^{-13}$	3.3 $\times 10^{-08}$
330101	flow1	46.3	47.1	0.846 $\times 10^3$	600	4.59	4.0 $\times 10^{-13}$	3.3 $\times 10^{-08}$

tural parameters are given. The relationship is described by

$$k(\phi) = C(\phi - \phi_{cr})^\mu, \tag{4.9}$$

where C determines the magnitude of the estimated permeability. As mentioned in the introduction to this chapter, it is clear that in addition to porosity, microstructural parameters have to be taken into account when permeability values are estimated. The simple power law relation (4.9), however, does not include any microstructural parameters like formation factor or a characteristic length scale (see Chapter 4 and Chapter 6), and has therefore to be scaled to the magnitude of the measured data one wants to fit, using the constant C to replace these parameters. C has to be determined empirically.

The power law relation can hold true only for porosity values above, but still close to, the critical porosity ϕ_{cr}. I will address this issue in Chapter 5 where I interpret the divergence of permeability measurements from the theoretical curve obtained by Equation (4.9), by mainly qualitative microstructural observations. I then employ a
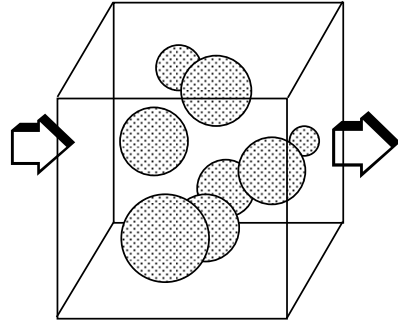
$$\phi_{cr} = 28.6 \pm 0.9\ \%$$

Figure 4.3: Spheres form a percolation pathway in the fully penetratable sphere model only if the critical porosity $\phi_{cr} \approx 30\%$ is exceeded.

more quantitative approach in Chapter 6 using the IAKC model.

The central idea in the application of percolation theory to permeability is that there has to be a minimum porosity below which no connected pathway for a fluid can exist. Imagine an impermeable cube of side length L. If permeable spheres with variable radii r, such that $r \ll L$, are randomly placed within the cube, it is necessary to add spheres until overlapping spheres form a connected pathway from one side of the cube to the other (see Figure 4.3).

The porosity ϕ can then be determined and is denoted as the critical porosity ϕ_c, or more generally the percolation threshold, the minimum porosity at which a pathway exists. It is clear that several calculations have to be carried out under same conditions in order to obtain an average value for such a percolation threshold. I wrote a C-program that determines critical porosities in two (2D) and three (3D) dimensions. The permeable objects used in these computer models are circles and ellipses in 2D and spheres and axisymmetric ellipsoids in 3D (Figure 4.3).
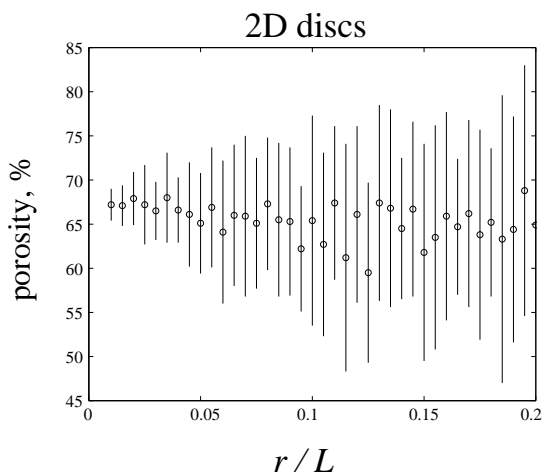
Figure 4.4: Critical porosity (percolation threshold) for the 2D disc model. Error bars are standard deviations based on 20 simulations. Calculations using a smaller radius have a smaller uncertainty but do not change the critical porosity value itself. The critical porosity is $\phi_{cr} \approx 68\%$. r is the disc radius, and L is the sidelength of the lattice.

4.4.1 Determination of Percolation Thresholds (ϕ_{cr})

2D-Disc (Circle)

I carried out several calculations with variable radii[2] such that $0.01 \leq \frac{r}{L} \leq 0.2$, where L is the sidelength of the continuous lattice and r is the radius of the object. In addition, calculations were carried out using two different radii arbitrarily. Results show that a decrease in radius decreases the uncertainty for the critical porosity determined by averaging several calculations. These calculations show, however, that different radii do not change the critical porosity value itself (Figure 4.4) even if two different radii are randomly used within the same simulation.

As a result, from this point forward, I use constant radii for critical porosity determinations. The resulting critical porosity for the smallest radius having the

---

[2]Typically simulations are repeated 10 to 20 times for a given percolation object geometry to determine average percolation thresholds and standard deviations.

smallest uncertainty is $\phi_{cr} = 67\% \pm 1.5\%$ which is in good agreement with commonly cited values of 68 % [Sahimi, 1995] for the fully penetratable disc model. The decrease of the critical porosity uncertainty stems from the fact that effects from the boundary of the lattice become less pronounced when the lattice is significantly larger than the percolation objects (see also Stauffer [1984]). This is analogous to saying that the characteristic length l_c has to be significantly smaller than the overall size of a sample[3].

3D-Sphere

These simulations are the 3D-analog of the 2D-disc model. The ratio of radius to lattice length ranges from $0.03 < r/L < 0.2$. As r/L decreases the uncertainty of ϕ_{cr} decreases as well (Figure 4.5). The resulting critical porosity however is only $\phi_{cr} = 28.6\% \pm 0.9\%$ which also is in good agreement with commonly accepted values of about 30% for the three-dimensional fully penetratable sphere model [Sahimi, 1995].

2D-Ellipse

Figure 4.6 shows the change of critical porosity with change of the aspect ratio of ellipses as percolation objects. For an aspect ratio of 1 (circle) the critical porosity is the same as in the 2D-circle model with $\phi_{cr} \approx 68\%$. The minor half axis is constant whereas the major half axis increases to the right to yield increasing aspect ratios. The elongation direction is oriented in percolation direction. The critical porosity decreases with increasing aspect ratio and asymptotically approaches a value slightly above 20 %.

---

[3]Imagine a square of side length $L = 10$ and a disc of radius slightly bigger than $r = 5$. Only one such disc placed in the center of the square would yield a critical porosity of $\phi_{cr} = \frac{\pi r^2}{L}$ which is approximately 79 %. If this disc is only slightly off-center, at least two discs are necessary to provide a connected pathway and the random position of their centers would largely determine if there is a connected pathway and what the critical porosity should be. ϕ_{cr} would thus reflect the random placement of disc centers in the square rather than the effect of the geometric structure of the percolation objects (here discs) on the critical porosity.
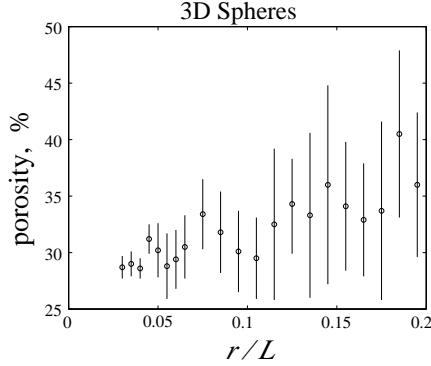
Figure 4.5: Critical porosity (percolation threshold) for the 3D-sphere model. Analogue to Figure 4.4, smaller radii decrease the uncertainty. The critical porosity decreases with decreasing radius and is $\phi_c \approx 29\%$. r = sphere radius, L = sidelength of the lattice.

3D-Ellipsoid

In contrast to the 2D-ellipse simulations, I observe an increase in ϕ_{cr} with an increase in aspect ratio (Figure 4.7). Here, the major to minor axis ratio varies while the intermediate axis stays constant. The longest axis is oriented in percolation direction. The ϕ_{cr} value for a sphere (aspect ratio = 1) is consistent with the 3D-sphere model ($\phi_c \approx 30\%$) which is a good check for the 3D-ellipsoid model.

A principle important difference between the 2D and the 3D models is that a sample spanning percolation pathway in the 2D system divides the impermeable matrix into two separate parts. The 3D system however is a bicontinuous system for pathway porosities between 30% (critical porosity) and 98%, where both media, the impermeable matrix and the permeable pathway are continuously connected [Sahimi, 1995]. This is observed in reticulite that shows porosities of up to 99 % [Mangan et al., 1996]. This fact is critical in later discussions.
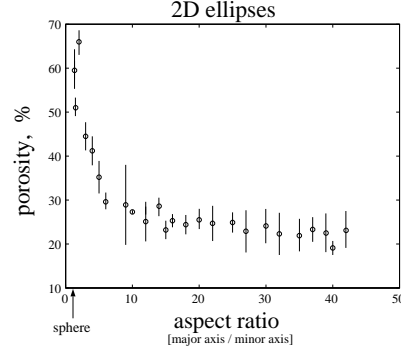
Figure 4.6: Critical porosity (percolation threshold) for the 2D-ellipse model. The uncertainty stays constant, wheras the critical porosity decreases with increasing radius to latice length ratio.
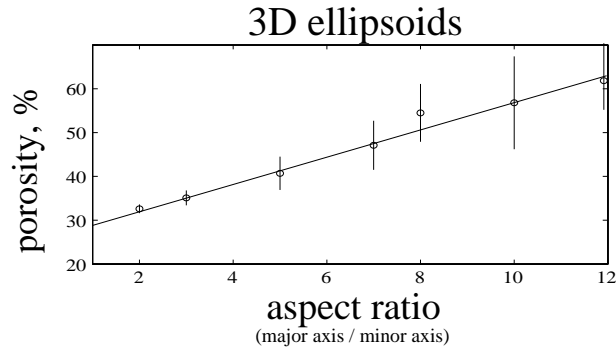
Figure 4.7: Critical porosity (percolation threshold) for the 3D-axisymmetrical ellipsoid model. The uncertainty and the critical porosity ϕ_{cr} decreases with decreasing half axis length aproching $\phi_{cr} \approx 30\%$ for an aspect ratio of 1 (sphere), the solution of the 3D-sphere model (Figure 4.5)

Chapter 5

Interpretations of Measurements Using Percolation Theory

In this chapter I interpret the measurements of Chapter 3 by using the percolation theory model introduced in Chapter 4. Chapter 6 then deals with permeability estimations using image analysis techniques and Kozeny-Carman equations (IAKC model) as proposed by the IAKC model, Chapter 4.

The larger the diameter of the tubes transporting fluid, the smaller is the inner surface area of the tubes per unit volume (specific surface area) for a given porosity. This results in less frictional force, easier fluid flow, and therefore higher permeabilities. I am interested in the relationship between the geometry of the pathway, the microstructure, and the permeability and not in the resistance to flow due simply to smaller tube radii. Permeability values are therefore normalized by dividing them by the characteristic cross sectional bubble area A_c of each sample (see Chapter 2 and Figure 2.6). Bosl et al. [1998] follow a similar approach for granular material by normalizing their permeability values by the sphere diameter squared to compare permeability values at different grain scales. Figure 5.1a and Figure 5.1b show unnormalized data for flow1, flow2 and scoria samples whereas Figure 5.1c and Figure 5.1d show the same data, with k normalized by A_c. The A_c used is indicated by a color

code.

I use Equation (4.6) together with the determined critical porosity $\phi_{cr} = 28.6\% \approx$ 30%, the exponent $\mu = 2$, and the scaling constant C to generate the percolation power law curve used for the graphs in this chapter. The solid curve represents the actual calculated values whereas the dashed curves indicate a factor of 5 deviation from the solid curve. The percolation theory equations involving a percolation threshold, such as the critical porosity, are valid only above, and close to, the percolation threshold itself. Since below the percolation threshold no connected pathway should exist, no significant permeability should be measured for porosities smaller than the critical porosity. However I will argue below how relatively high permeabilities can exist well below the critical porosity ϕ_{cr}, as shown in the data.

This assumes that for all sample types (scoria, flow1, and flow2) a connected sample-spanning pathway was achieved in the very early formation stage when all systems consist only of subspherical bubbles, and the porosity was above the critical porosity ($\phi_{cr} \approx 30\%$). I carried out percolation theory simulations where the porosity was increased above ϕ_{cr}. These calculations show that a minimal porosity increase above ϕ_{cr}, approximately 1 %, yields a bicontinuous percolation system, in which both the permeable and the impermeable media are continuous. This is in good agreement with Sahimi [1995]. Therefore virtually all bubbles are connected (Figure 2.5) at $\phi > \phi_{cr}$. If the assumption of bubble coalescence during the early emplacement stage is correct, then the 3D-sphere percolation model and its critical porosity of about 30 % may be the appropriate one to determine the percolation threshold for scoria (spheres), flow1 (ellipsoids) and flow2 (collapsed ellipsoids) samples. This assumption is probably realistic, because the subspherical bubbles in scoria are mostly connected (see Figure 2.5). Bubble elongation as shown in flow1 and flow2 samples and bubble collapse as shown in flow2 samples probably occur at a later stage causing a secondary
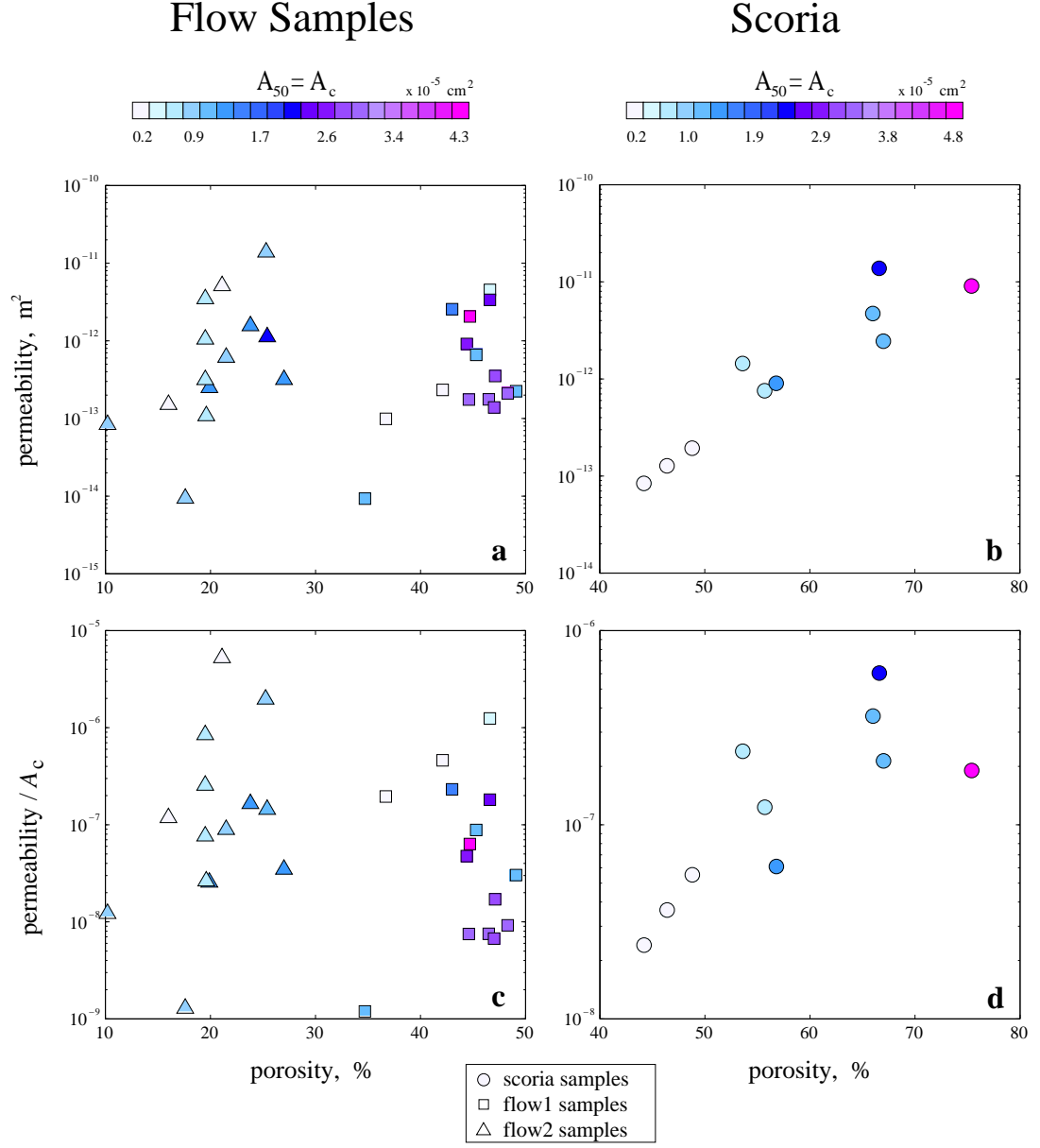
Figure 5.1: a) and b) ϕ-k relationship of scoria, flow1 and flow2 samples. c) and d) k normalized by characteristic area A_c.

change of permeability and porosity values. Figures 5.3, 5.6, and 5.7 show the curves obtained this way together with the normalized data for the scoria and flow1 samples.

5.1 Scoria and Flow1 Samples

The unnormalized scoria data show an increase in permeability with an increase in porosity that is accompanied by an increase in characteristic bubble size (Figure 5.1b). However when the data points are plotted on a graph where the permeability is normalized by characteristic bubble size (cross sectional surface area), one can see that the points plot approximately on a horizontal line indicating only minimal permeability increase with increasing porosity (Figure 5.1d). This indicates that the permeability increase is mostly governed by an increase in average bubble size leading to less viscous resistance due to smaller specific surface areas. Subspherical bubbles are formed during the early emplacement stage of both cinder cones and flows. These bubbles grow due to decreasing pressure and continued degassing during magma ascent [e.g. Mangan and Cashman, 1996]. Figure 2.5 shows that practically all bubbles (scoria and flows) are connected so that I know that these bubbles coalesce and form apertures. Rapid cooling, however, prevents further aperture widening in cinder cone scoria. Scanned images of cinder cone cores show that bubbles deform each other (Figure 5.2) rather than completely draining the thin film in between them which requires slower cooling rates.

I call this effect of reduced interbubble film relaxation "impeded aperture widening". The shape of the bubbles reflects deformation due to bubble expansion rather than elongation due to shear flow. Bubbles preserve their subspherical shape to a large degree due to rapid cooling (chilling), low viscosities and high basalt-gas surface tension (see chapter IV). This results in low average roundness numbers between $R_{\mathrm{round}} = 1.26$ and $R_{\mathrm{round}} = 1.57$ (see Figure 3.5) where $R_{\mathrm{round}} = 1$ indicates a perfect
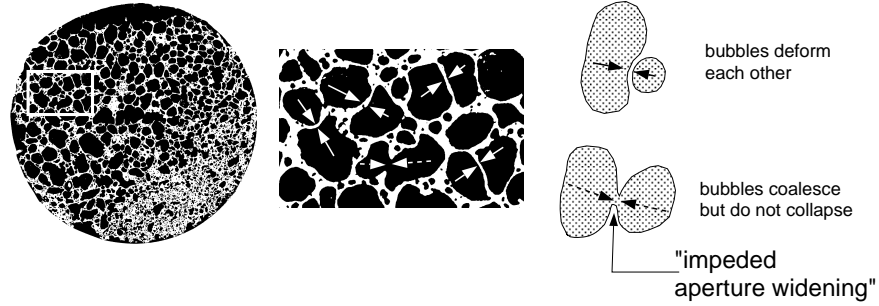
Figure 5.2: Impeded coalescence and aperture widening of bubbles in scoria samples due to rapid cooling rates which prevents the thin lava film in between bubbles to drain significantly. Interbubble apertures are small and might not be shown in an arbitrary cross section. However, bubbles deforming each other does not indicate a lack of coalescence between these particular bubbles.

sphere.

The processes leading to the shape and geometry of the permeable pathways in scoria samples are the ones that are best reflected by the percolation theory power law curve I used. The 3D-sphere percolation model uses spheres as percolation objets and assumes a connection between two spheres with radius r that develops as soon as the spheres overlap (distance between sphere centers $< 2r$).

The 100 % connectiveness of the pores argues for relatively easy coalescence of the bubbles and the subspherical bubble shape implies early quenching of the lava preserving this initial coalescence stage and impeded aperture widening. The porosity (total=accesible) is higher than the critical porosity calculated in the 3D-sphere model allowing all bubbles to be connected. This is observed in my percolation simulations as well. The models I calculate indicate that a small further porosity increase beyond the critical porosity ϕ_{cr} by approximately 1 % (adding more spheres in the model) results in a connection of all bubbles. This agrees with Sahimi [1995] who states that both media (the permeable and the impermeable) in a fully penetratable 3D-sphere

58

model are completely connected (bicontinuous system) for porosities between 30 and 98 %. Only the 3D case of the fully-penetratable sphere model is bicontinuous. This observation explains the high pore space connectivity (100%) of vesicular materials once the porosity exceeds the critical porosity of about 30 % which is the case for all scoria samples.

The model further assumes that the impermeable matrix really is completely impermeable and that no micropore permeability exists. All fluid is assumed to flow through the macropores. This again is true for the scoria samples which show a glassy impermeable matrix surrounding the vesicles and mostly true for the flow1 samples.

Figure 5.3 shows the power law curve obtained by the fully penetratable 3D-sphere model. Flow1 samples are plotted together with scoria samples in Figure 5.3 since their textures and bubble geometries are very similar: Both have a glassy, predominantly impermeable matrix (see thin section images in Figures 3.2 and 3.3), a pore space connectiveness of 100%, and smooth, round (see Figure 3.5) subspherical (scoria) or ellipsoidal (flow1) bubbles (for comparison see also Table 4.1).

The curve is scaled to the measured permeability values. This is necessary in simple power law $\phi - k$ relations since no microstructural parameters are taken into account. The magnitude of the percolation curve therefore falls in the right range. The shape of the curve, however, and its predictions for k is of interest here and is defined by the critical porosity, ϕ_{cr}, the exponent μ and the power law, Equation (4.9). The solid line is the actual curve whereas the dashed lines indicate a factor of five deviation from that curve. Blair et al. [1996] obtain a deviation of a factor of two to three in their IAKC model. The Scoria samples fall within this range as well as most of the flow1 samples. However it can be observed that the flow1 samples, on average, are more permeable than the scoria samples for a given porosity which reflects an important difference despite their similarities. Flow1 samples contain
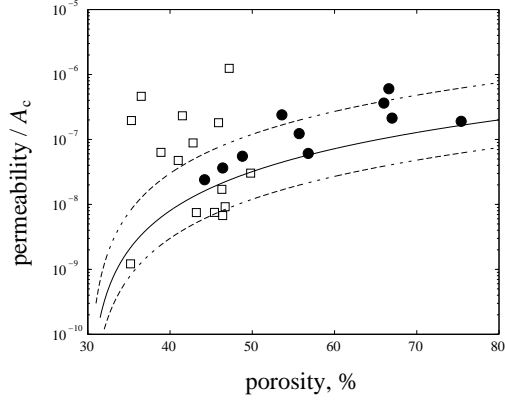
Figure 5.3: ϕ-k relationship (normalized) for scoria (filled circles) and flow1 (open squares) samples. Here $\phi_{cr} = 30\%$ and $\mu = 2$ [Sahimi, 1995]. The curve is valid only close to ϕ_{cr}, but has been extended to $\phi = 80\%$.

elliptical bubbles of an aspect ratio of about 2 to 3 as a result of shear flow elongating the bubbles in flow direction [Polacci et al., 1997; Polacci and Cashman, 1998]. The pore space connectiveness is 100 % for both scoria and flow1 samples, the slower cooling rates allow more time for drainage of the thin film separating two bubbles and therefore causes interbubble aperture widening (see also Chapter 5). I expect that the interbubble aperture size determines largely the resistance of the pathway network towards fluid flow and not the inter aperture bubble size. On average larger apertures therefore yield higher permeabilities[1] for given porosities.

5.2 Flow2 Samples

It is likely that flow2 samples represent a more developed stage of the crystallization and deformation process noticed in flow1 samples. The longer cooling time allows further deformation and drainage of the thin film separating bubbles, and therefore,

---

[1] An additional factor increasing permeability might be the existence of intercrystalline micropores in a beginning dictitaxitic texture due to some crystal growth. However this effect can probably be neglected since the predominantly glassy matrix fills micropores.

widening the interbubble apertures resulting in an increase of the overall permeability of the system. The matrix finally reaches a holocrystalline, diktytaxitic texture in which the intercrystalline micropores might allow additional fluid flow increasing the permeability. However, permeability measurements on flow2 samples containing only micropores show permeabilities on the order of 10^{-17} m^2 and can therefore be neglected when compared to measured permeabilities in the range of $10^{-14} < k < 10^{-12}$ m^2. The enhanced permeability due to aperture widening, however, permits the escape of gas from bubbles leading to bubble collapse and a decrease in total porosity (Figure 5.4). Aperture widening, however, is not as pronounced in flow1 samples as in flow2 samples. Flow1 samples reflect the initial stage of a basalt flow emplacement and are relatively rapidly cooled resulting in properties more similar to the quenched scoria samples though indicating the beginning of aperture widening when slower cooling rates are present. Scoria samples on the other hand show impeded aperture widening.

The measured accessible (connected) porosity of flow2 samples showing collapsed bubbles is still as high as the total porosity but significantly below the critical porosity ($\phi_{cr} \approx 30\%$). An explanation for this could be provided by the idea that a fully connected pathway network formed at the very early 3D-sphere stage of the system when the porosity exceeded the critical porosity. This network is preserved even when vesicles collapse (Figure 3.4). Although surprising at first, it is reasonable considering the fact that the fully penetratable sphere (or ellipsoid or pathway) model is bicontinuous (see introduction to this chapter) and all pores are connected once the critical porosity is exceeded by only a small amount (about 1 %). This must have been the case for the flow2 samples before their permeability increased so much, due to aperture widening, that gas escaped and the bubbles collapsed. Closing such a complex network of branching and connected pathways at some locations is very unlikely to
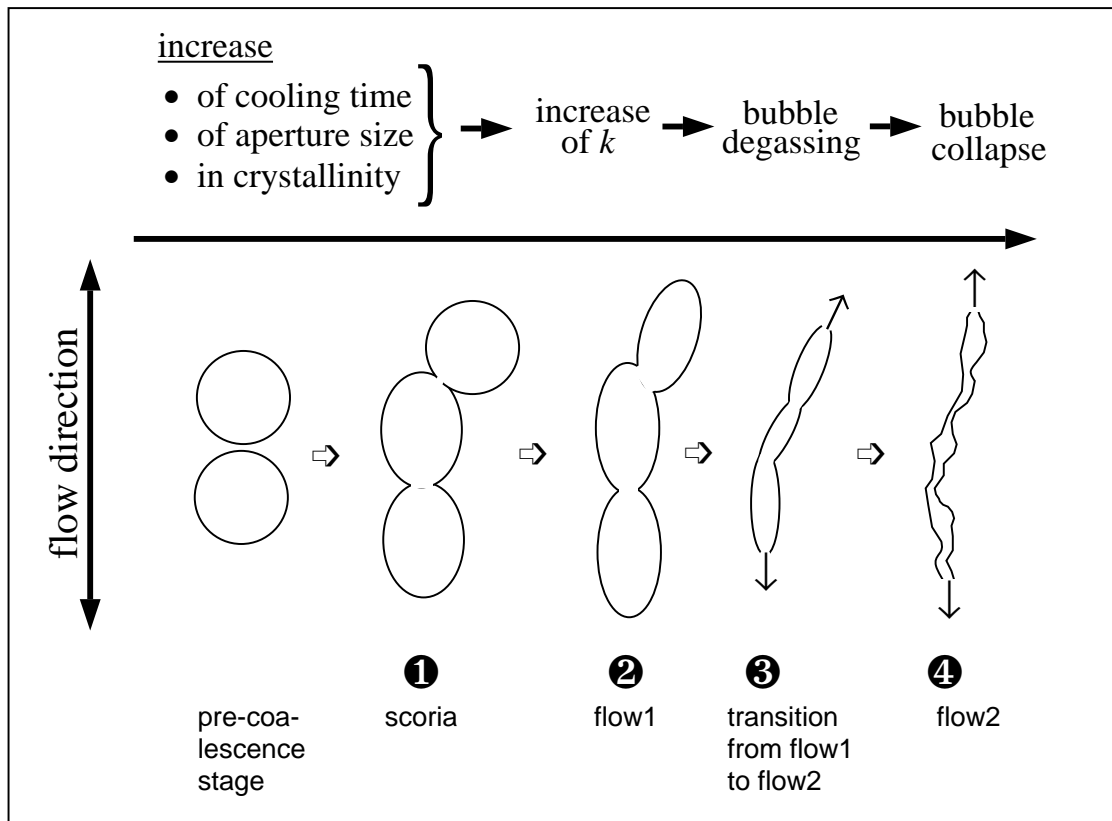
Figure 5.4: Bubble degassing and collapse. From left to right the cooling rate decreases allowing more crystal growth and aperture widening (flow1 samples) which leads to higher permeabilities in elongation (flow) direction. This in turn allows gas to escape from the bubbles which then "collapse" (flow2 samples).
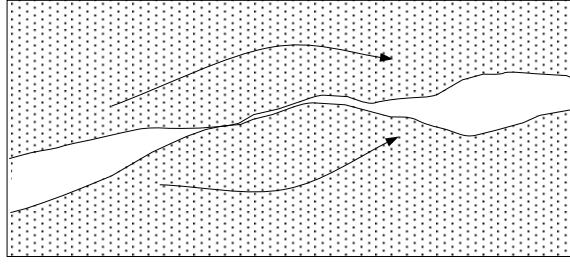
Figure 5.5: Micropore bridging over collapsed bubbles

form isolated pores. The resulting elongated pathways (Figures 5.44, and 3.4) show a more consistent width than the overlapping bubbles forming small apertures in scoria or flow1 samples (Figure 5.4 stage 1 and 2, Figure 3.2 and Figure 3.3). The fluid flow in flow2 samples is therefore less impeded, while the porosity is decreased by a large degree.

In addition, it is probable that completely closed pathways are bridged by micropores (Figure 5.5). Flow2 samples therefore can have relatively high permeabilities for porosities well below the percolation threshold of $\phi_{cr} \approx 30\%$, where k should be virtually zero (Figure 5.6). Permeability values in Figure 5.6 are normalized by A_c. The permeability decrease accompanied by a decrease in cross sectional area (higher specific surface area) due to bubble collapse is therefore taken into account.

In summary, it can be observed in Figure 5.7, that flow2 samples show a counter-intuitive trend of decreasing bubble size and porosity (total = connected) while their normalized permeability stays constant or even increases slightly as a result of microporosity. This trend leads to a deviation away from the predicted percolation curve (Figure 5.7a and Figure 5.7b) allowing high permeabilities for porosities below the critical porosity ($\phi_c \approx 30\%$) where no connected pathway should exist and k should be close to zero. Figure 5.7 shows this trend for normalized data. Unnormal-
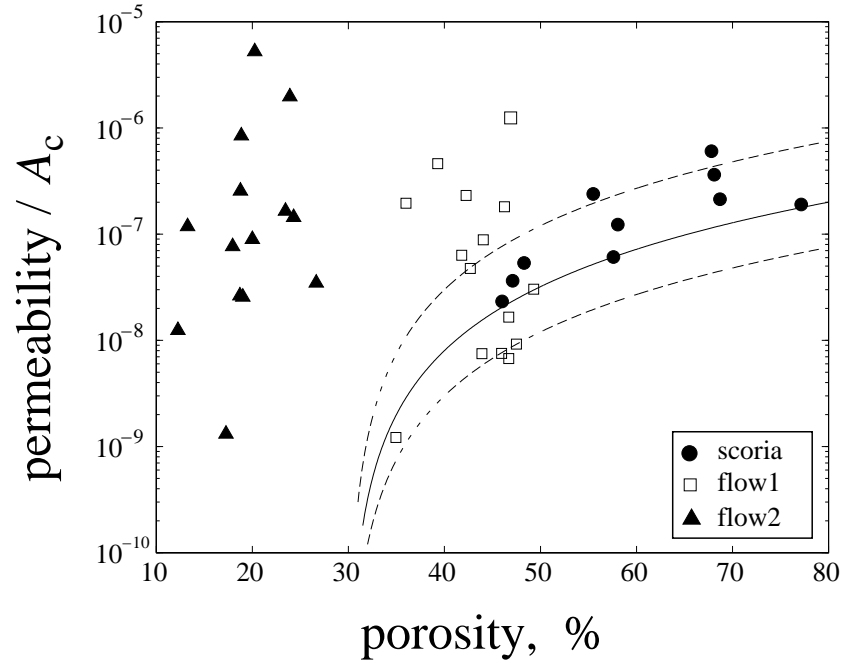
Figure 5.6: Normalized ϕ-k relationship for scoria, flow1 and flow2 samples. A_c is the characteristic cross sectional bubble area of a sample. Scoria samples follow the trend suggested by percolation theory relatively well, whereas flow1 samples deviate from it to a larger degree. Flow2 samples do not follow the curve at all, but show relatively high permeabilities for $\phi < \phi_{cr}$, where k should be close to zero.

ized data (Figure 5.1a) shows a less pronounced trend, since smaller (collapsed but connected) bubbles decrease the permeability due to increased viscous resistance per bubble cross sectional area. In addition, the higher intercrystalline microporosity in basalt flows might increase the permeability values as well. However this effect can probably be neglected, because, as mentioned previously, samples containing micropores have permeabilities of about 10^{-17} m^2.
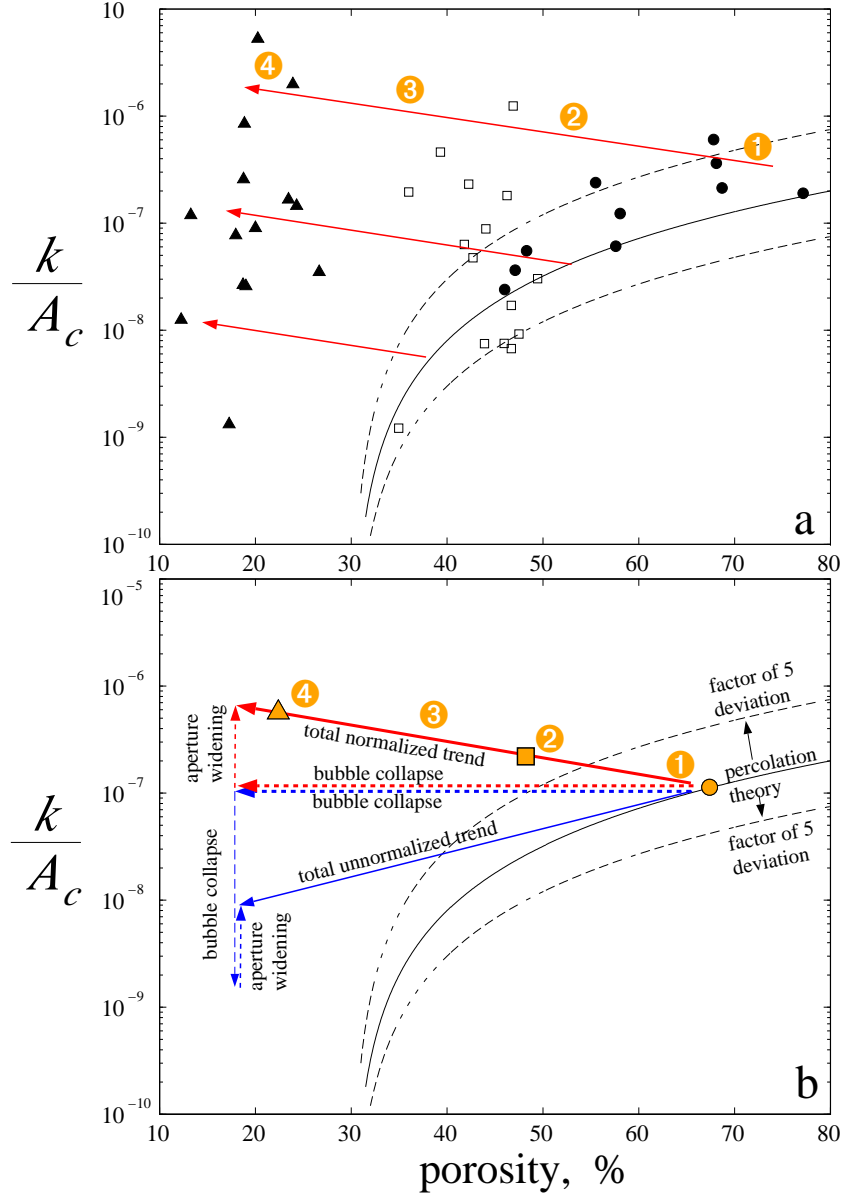
Figure 5.7: Divergence of flow samples from percolation theory model. Flow2 samples (stage 4) cooled relatively slowly which is reflected by the high crystal abundance. Therefore relaxation of the thin film between bubbles is possible, widening the interbubble apertures and leading to an increase in permeability. The enhanced permeability allows degassing of bubbles which in turn leads to bubble "collapse". The overall counterintuitive effect is a pronounced decrease in porosity below the critical porosity of $\phi_{cr} \approx 30\%$ accompanied by a normalized permeability increase due to high pathway connectiveness.

Chapter 6

Permeability Estimations Using Kozeny-Carman Equations

In this chapter I estimate the permeability of vesicular basalt samples using the IAKC model (Chapter 4). I compare these estimated permeabilities with permeability measurements (Chapter 3) and with interpretations based on percolation theory (Chapter 4) and porosity measurements.

6.1 Method of Calculating Permeability

Kozeny-Carman equations [Carman, 1956; Dullien, 1979] can be used to estimate permeability when the specific surface area (surface area of the bubble-rock interface per unit volume), the formation factor F and the porosity of the sample are known. This approach has so far been mostly applied to approximately homogeneous granular materials such as welded glass beads and Berea sandstone [e.g. Berryman et al., 1996].

Here I apply these ideas to less homogeneous (partly anisotropic) vesicular basalt. I measure specific surface area using two-point correlation functions (Chapter 2) and determine the formation factor using Equation (4.8). Total porosity and accesible porosity were determined using the methods described in Chapter 2 and 2, respectively. In addition I computed total porosity, using a one-point correlation function, see Chapter 2 and Equation (2.18), which provides an estimate of the real porosity
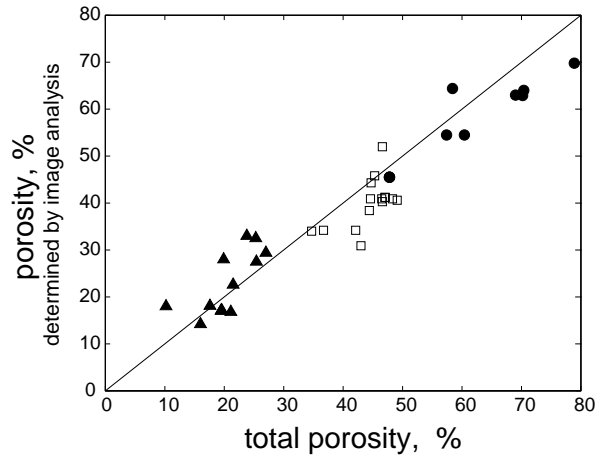
Figure 6.1: Comparison of total porosity measurements. The integrated method (sse Chapter 2) is more accurate than the image analysis method, because it uses the whole sample to determine the porosity and not just a cross sectional image. It can be observed that the two methods yield different results which is a measure of the extent to which the cross sectional image is representative (filled triangles: flow2 samples, open squares: flow1 samples, filled circles: scoria samples).

because only a cross section of the total core is used rather than the whole core. Nevertheless it provides indication of how representative such a cross sectional area is for the whole core sample which is important since the same cross sectional image is used for the determination of the specific surface area in two-point correlation functions (Chapter 2). Figure 6.1 shows the relationship between measured integrated porosity and the cross sectional porosity measurement.

Figure 6.1 shows that the samples are relatively heterogeneous, since samples deviate by a considerable amount (but less than 10 %) from the line indicating same porosity values for both methods. This heterogeneity was observed in the field and in handsamples and causes difficulties in permeability estimation. Therefore, I tried to choose samples that are as homogeneous as possible. In contrast to total porosity determination where I apply two methods and choose the much more accurate

integrated porosity measurement value as porosity data base I can only obtain specific surface area values by using a representative cross sectional images for two-point correlation functions. Therefore it can be expected that the surface area is only a particular value of a core cross sectional area and may vary throughout the more or less heterogeneous cores. Gas absorption methods provide a much more accurate surface determination. However the two-point correlation method was chosen since it provides a smoothed estimate of the bubble surface area which is, according to Berryman et al. [1987], the one necessary for Kozeny-Carman equations (see also Chapter 4), though the Kozeny-Carman equation itself depends on idealized parallel tubes representing the complex real pathway system of a rock. Berryman et al. [1987] also stress that permeability estimations deviate increasingly with increasing heterogeneity.

6.2 Comparison of Calculated and Measured Permeability

Figure 6.2a shows calculated permeability values for the 39 samples. The calculated permeability values are systematically higher for flows (flow1 and flow2) than for scoria samples which is due to the larger bubble sizes in flows. Once the calculated permeability is normalized by characteristic bubble cross sectional area (Figure 6.2b), the distinction between cinder cones and basalt flows is not as pronounced.

The smaller cinder cone vesicle sizes, compared with basalt flow vesicles, lead to a larger number of vesicles in cinder cones than in basalt flows for a given porosity. This in turn results in larger specific surface areas for cinder cone samples, despite their higher roundness. The distinct curves for cinder cone and basalt flow samples in Figure 6.2a and the common curve for both sample types in Figure 6.2b is therefore expected.
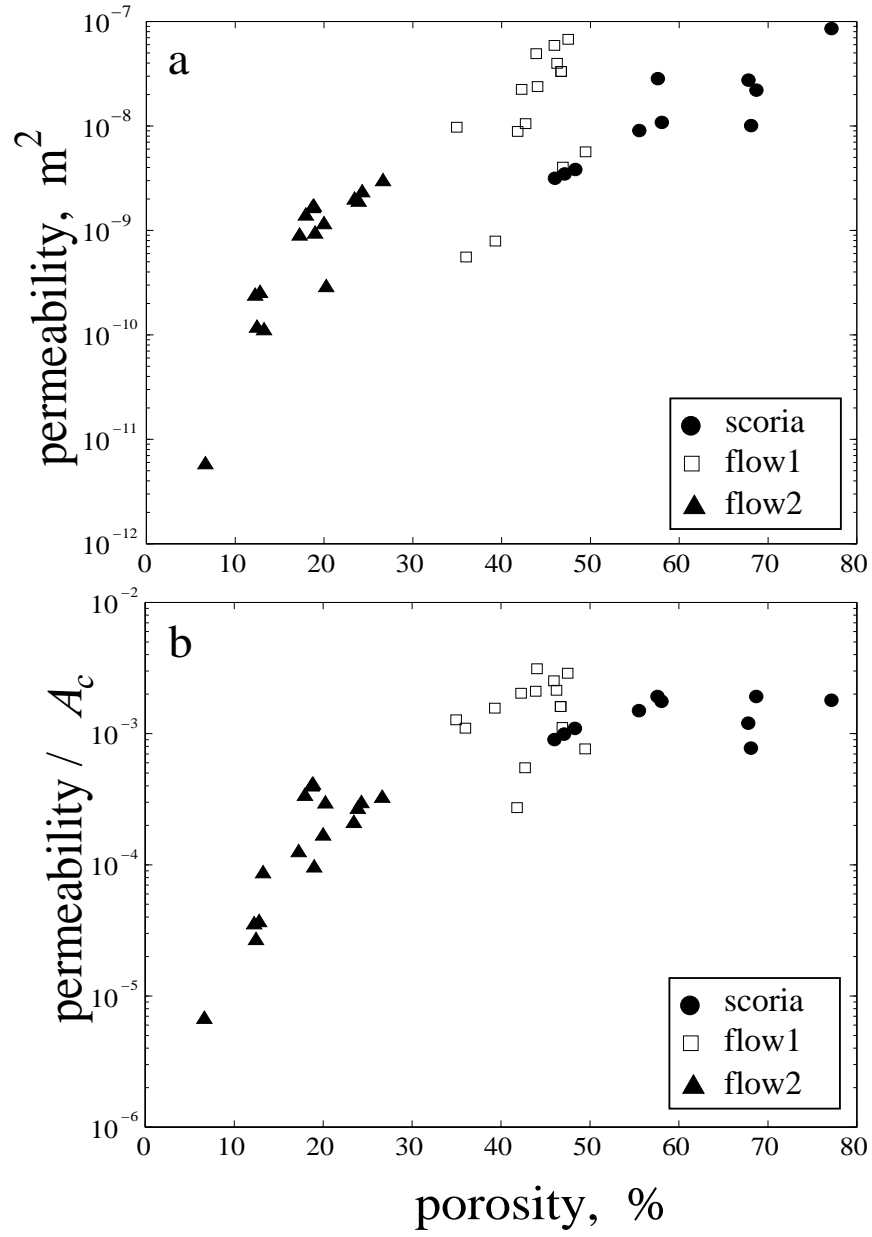
Figure 6.2: Calculated permeability using the IAKC model. a: k is not normalized, b: k is normalized by the charcteristic cross sectional bubble area A_c.

The strong impact of porosity on permeability estimates is evident in Equation (4.6). It becomes more obvious when Equation (4.8) with an exponent of $m = 1.5$ (for very round bubbles) is substituted into Equation (4.6)

$$k = \frac{\phi^{3.5}}{cs^2} \tag{6.1}$$

Even higher porosity exponents, up to 2 in Equation (4.8), are expected for less round bubbles [Archie, 1942; Sen et al., 1981; Blair et al., 1996]. Therefore permeability is more sensitive to porosity than specific surface area, when Equation (4.8) is used to obtain the formation factor.

When I compare calculated and measured permeability (Figure 6.3) it can be observed that the calculated permeabilities are systematically higher than the measured ones by several orders of magnitude.

A contribution to the lower measured permeability values could be that the equivalent channel model [Paterson, 1983] assumes cylindrical tubes of a cross sectional tube area similar to the average cross sectional void area in the images. Again this assumption is more likely to hold true for granular material where cross sections through intergranular necks (Figure 6.4a) are more representative of the equivalent channels, despite being subject to large variations, than cross sections through bubbles in vesicular basalts. Permeability of vesicular material is largely determined by the even wider range of, but on average far smaller, aperture sizes formed by overlapping penetratable spheres or ellipsoids (Figure 6.4b) (fully penetratable sphere or "inverted Swiss cheese" model [Feng et al., 1987], rather than by the whole bubble cross section (which is the measured one). The effective tubular cross sectional area is therefore likely to be overestimated by a large degree in vesicular basalt images, even though arbitrary cross sections through spheres usually do not show the full sphere

71
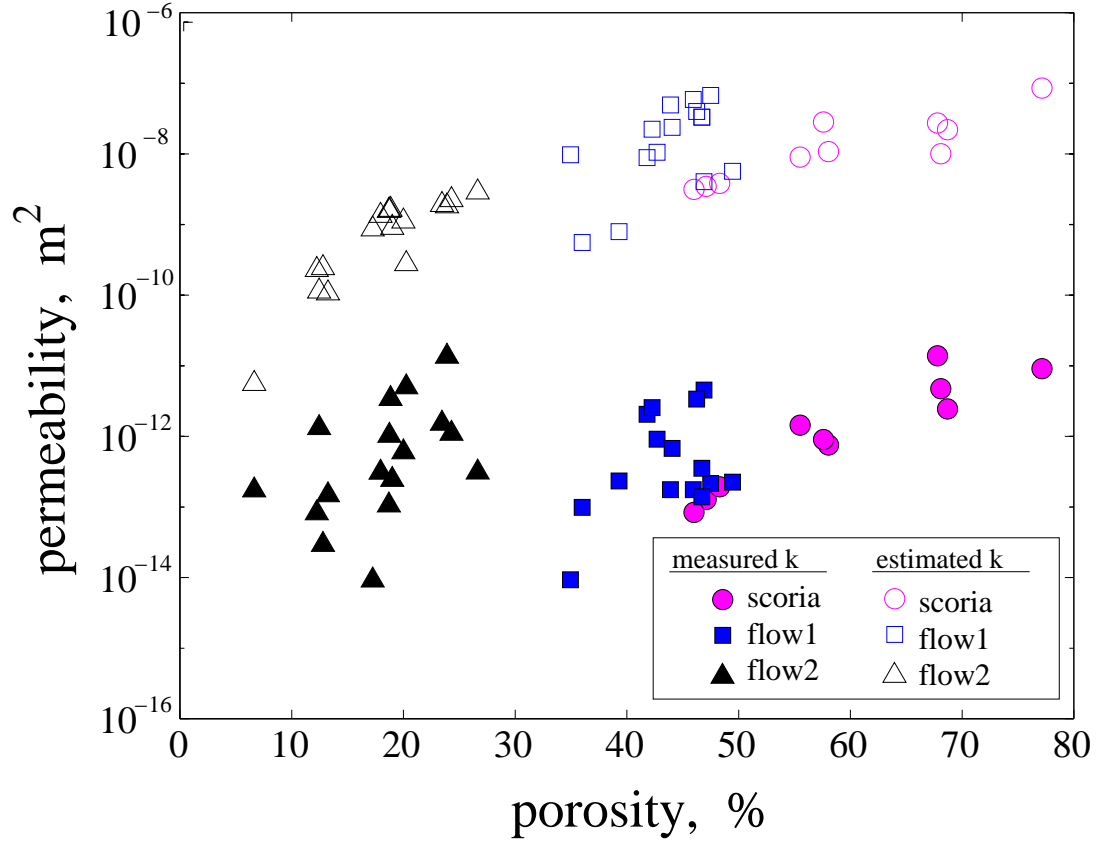
Figure 6.3: Calculated and measured permeability (not normalized). The calculated permeability for a given porosity is about four orders of magnitude higher than the measured permeability. This overestimation of permeability could be a result of insufficient interbubble aperture resolution of the images. The small apertures determine the permeability rather than the large bubbles in between the apertures (see Figure 6.4). These large bubbles, however, are mainly resolved in the images and therefore used for specific surface area determinations in two-point correlation functions. However, the shapes of the trends (calculated and measured k) show similarities, indicating a possible use of the IAKC model for vesicular basalt, if the fluid flow determining aperture sizes are resolved. Flow2 samples show a smaller overestimation of approximately three orders of magnitude, which indicates a larger aperture over bubble size ratio and therefore slightly better flow pathway representations in these images.
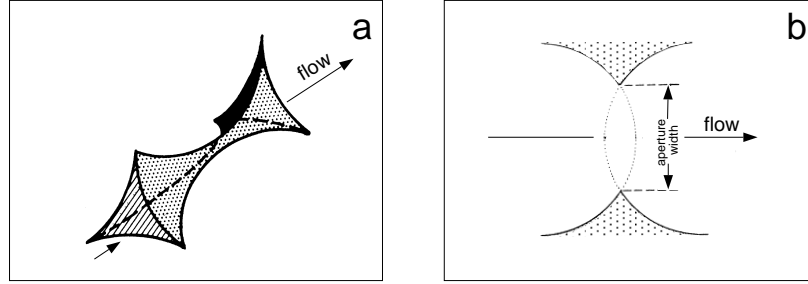
Figure 6.4: The neck and overlapping spheres models. The two different fluid flow pathways. a) fluids flow through narrow necks in between impermeable spheres (e.g. granular materials). b) fluids flow through permeable spheres, i.e. the fully penetratable sphere model (modified from Feng et al., 1987). The small interbubble aperture size determines largely the material's fluid flow properties, such as permeability, rather than the large bubbles themselves.

diameter or cross sectional area.

Permeability estimations are still about four orders of magnitude too high. This large discrepancy is probably the effect of a significantly smaller aperture size of overlapping ellipsoids than the average size of the ellipsoids. It is not possible, however, to account for this effect using image analysis techniques, to determine the parameters for the Kozeny-Carman equation. A different method seems to be needed to estimate permeability in vesicular materials. In my concluding remarks I suggest a method that might be appropriate to address the noted complication.

The collapsed bubbles of the flow2 samples (Figure 3.4 and Figure 5.4 stage 4) represent the average pathway properties slightly better than the uncollapsed bubbles in flow1 and scoria samples, since apertures in flow1 samples are widened (closer to the granular material geometry). However, the predominantly non-elliptical, very narrow and stretched pore spaces observed in flow2 samples are difficult to resolve with image analysis techniques. This can be seen in table T3 where the maximum

resolution capacity of 1200 dpi is not sufficient for some of these flow2 samples. An increase in resolution above 1200 dpi is expected to yield an increase in specific surface area (similar to the granular material case). An underestimation in specific surface area however results in an overestimation of permeability. The effects of more appropriate pathway geometries (decreasing k estimates) but too small resolutions (increasing k-estimates) may cancel out each other.

6.3   Conclusions Involving Kozeny-Carman Equations

The Kozeny Carman equation that is based on the equivalent channel model [Paterson et al., 1983] (Equation 4.6) relies on the correct determination of the channel cross-sectional properties which are expressed in terms of porosity and specific surface area of a material. Ideally the samples should be homogeneous, all pores should be connected and if image analysis is used, an image from a sample cross section should exhibit an average range of pore cross sections that determine the fluid flow properties of the medium. In vesicular materials however the inter-bubble apertures which largely determine the material's permeability are by far smaller than the measured average inter-aperture bubble size. The average aperture size cannot be resolved with image analysis techniques. Therefore the aperture sizes remain overestimated by a large degree leading to permeability overestimations by about four orders of magnitude.

It might be possible to adjust the equation by simply dividing the k-estimates by this factor. This however requires actual initial permeability measurements of the material in question in order to obtain that factor and is therefore not particular useful (except for the case when many k-data of roughly the same material are needed and can't be carried out easily). It is also not clear at this point how this factor might

74

change from one location within a lava flow to another, since it reflects the average aperture size (average overlap of bubbles).

I therefore conclude that the IAKC-model is not appropriate for k-estimations of vesicular materials where the vesicles accommodate fluid flow, even though it seems to work for the inverse case of fluid flow around impermeable spheres (granular materials).

Chapter 7

Concluding Remarks

Bubbles forming in cinder cone scoria are best characterized by the fully penetratable sphere model. Aperture widening is impeded due to rapid cooling, and thus does not allow the thin interbubble film to fully retract. Permeability values therefore plot close to the theoretical porosity-permeability relationship curve determined by the percolation theory approach.

Because the porosities of scoria samples are greater than the critical porosity of $\phi_{cr} \approx 30\%$ almost all pores are connected. The scoria bubble-matrix system is therefore a bicontinuous system in which both the impermeable matrix and the permeable pathways are continuous (no isolated "islands"). This is also confirmed in percolation simulations in which a slight increase above the critical porosity leads to a fully connected pathway system.

The high crystallinity of some basalt flow samples (less pronounced in flow1 than in flow2 samples) indicates slow cooling rates which allows the widening of "narrow" pathways (apertures) between bubbles. This leads to smaller specific surface areas of the critical narrow pathways (apertures), increases the overall permeability, and allows gases in the bubbles to escape (flow2 samples only). As a consequence, bubbles in flow2 samples seem to "collapse" resulting in a decrease of porosity and permeability. Normalizing permeabilities by the smaller characteristic pathways (bubble cross

sectional area A_c), however, accounts for the effect of k decrease due to narrowing. This results in an increase in normalized k. Flow2 samples therefore show relatively high permeabilities for porosities significantly below the critical porosity of $\phi_c \approx 30\%$.

Similar to the scoria samples, flow samples (both flow1 and flow2 samples) also contain fully connected pore spaces and therefore also represent a bicontinuous system. This is true even for flow2 samples containing collapsed bubbles indicating that the closing of some pathway locations does not prevent the complex pathway network, that was formed at an early stage of high porosities, from being totally connected.

It is important to note that the percolation theory approach does not offer a scaling possibility, as it lacks parameters like the formation factor or the characteristic length. Some measurements therefore have to be carried out in order to scale the calculated power law curve to the necessary magnitude (see Chapter 4). However, it provides a description of a porosity-permeability relationship and thus provides a framework for interpreting measurements. Therefore it can potentially be used to gain a qualitative understanding of processes associated with vesicular basalt formation.

In order to determine a porosity-permeability relationship for vesicular basalts it is necessary to account for emplacement mechanisms and microstructures. Percolation theory concepts using a power law relationship and the idea of a percolation threshold (here critical porosity) provide an adequate correlation between porosity and permeability around ϕ_c only if bubble collapse can be neglected and interbubble aperture widening is not very pronounced (scoria and to a certain degree flow1 samples).

Image-analysis techniques can probably not be used for Kozeny-Carman equation parameter determination for vesicular materials since the average interbubble aperture size is not resolved with such a technique. A self-scaling method, not relying on a scaling constant, e.g. percolation models, is therefore lacking.

Vesicular materials probably require the development of a more dynamic model that uses emplacement mechanisms and processes (e.g. vesicle nucleation, grow, deformation, degassing and collapse) to generate a 3D-image of overlapping "ellipsoids". The simulation can be performed until the boundary conditions (total and accessible porosity and average ellipsoid aspect ratio) are achieved. The analysis of this 3D-image might be more appropriate to estimate the permeability of vesicular basalts since the average aperture size of overlapping ellipsoids can be calculated and be used as the characteristic tube size in the equivalent channel version [Paterson et al., 1983] of the Kozeny-Carman equation (Equation 4.6).

Appendix A

Constraints on Radius Minimization in the Percolation Theory Model

Although I am using a continuous model with object centers and axis-lengths being real-valued numbers, it is necessary to discretize the lattice to calculate the critical porosity once a percolation pathway is achieved. However, calculations to check for a connected pathway are done on undiscretized continuous objects. Discretization places constraints on the minimum bubble size, since the round objects have to be approximated by discrete squares (2D) or cubes (3D) of sidelength $L = 1$. It is necessary to minimize the percolation object size with respect to the lattice size while keeping it large enough so that discrete cube elements allow appropriate estimations of the critical porosity ϕ_{cr}.

The only possibility to achieve the two conditions of having small enough percolation objects within the lattice and having large enough objects that can be sufficiently approximated by discrete cubes is to increase the lattice size. I am using a 1000×1000 continuous square in 2D and a $1000 \times 1000 \times 1000$ continuous cube in 3D, while radii (or percolation object half axes) are typically around 10 length units. It would require 50 (for $r = 10$) perfectly aligned circles/spheres to form a pathway from one

side of the cube to the other when using these dimensions. Since this is statistically extremely unlikely to happen, typical sphere numbers range from 2000 to 3000 at the percolation threshold. To obtain an average critical porosity and a standard deviation, I typically carry out 10 to 20 runs for each porosity-determination for a given object geometry and size. The chosen dimensions of the lattice and the object sizes and the 10 to 20 run repetitions require on the order of 10^{9-11} calculations in order to check for a connected pathway and for calculating porosity, leading to calculation times for critical porosities on the order of 2 to 10 days on an Ultra Sparc II (Sun) work station. Improving the program (simplifying algorithms, upgrading to C^{++} and parallel processing) is therefore necessary in order to be able to conduct dynamic percolation models that include various ellipsoid orientation and bubble collapse processes due to degassing (see later). However the work done so far can already provide useful information about critical porosities of the basalt samples.

Appendix B

Core Images

In order to conduct image analysis calculations, it is necessary to prepare the core cross sectional discs for scanning purposes. The pores are first filled with spray paint to access very small pores and then with plaster to completely fill large voids. The surfaces are polished to eliminate surplus paint on non-void rock faces and then spray-painted with a clear lacquer to enhance the black (rock) and white (voids) contrast. The rock discs are then directly scanned at 1200 dpi resolution and inverted so that the voids are black and the rock is white to achieve a binary image.

Some permeability measurements are carried out on different sections of a rock core. The image used for image-analysis purposes is the same in these measurements, because the cross-sectional characteristics should be similar for the different sections of the same core. Some images are therefore duplicates of another.
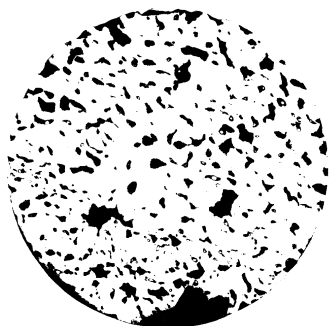
b003-01
(301)
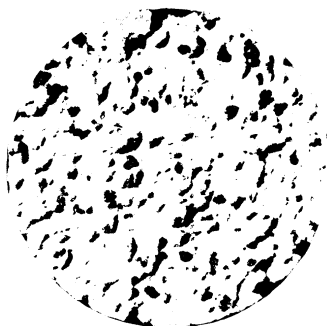
b003-02
(302)
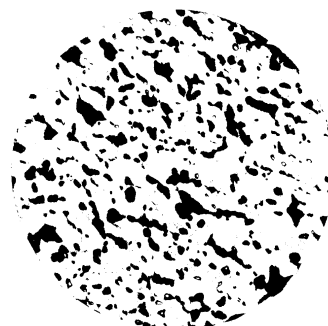
b003-03
(303)
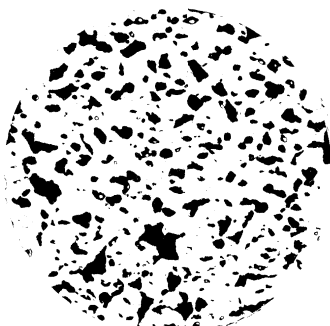
b003-04
(304)
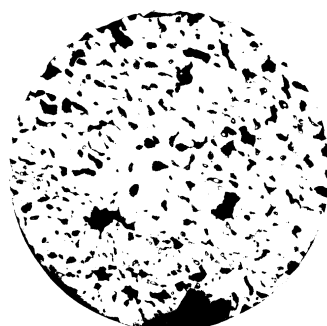
b003-01-A
(30101)
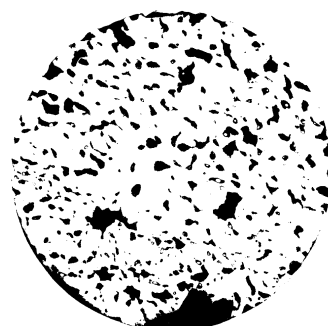
b003-01-B
(30102)
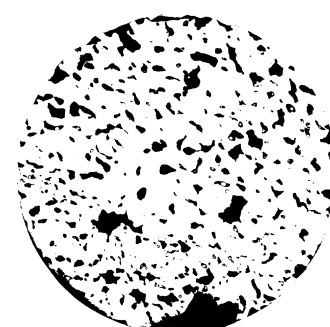
b003-01-C
(30103)
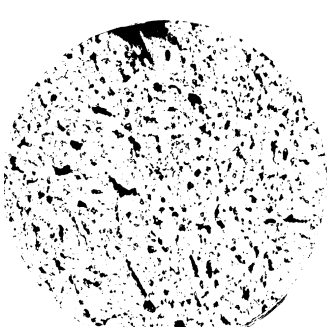
b004-02
(402)
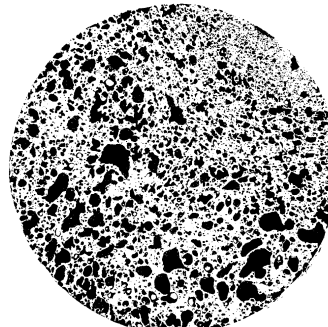
b005-01
(501)
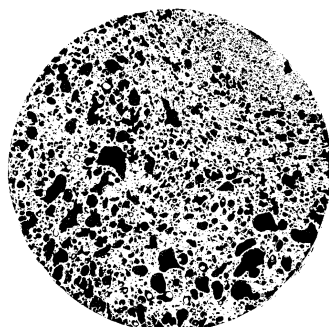
b005-01-A
(50101)
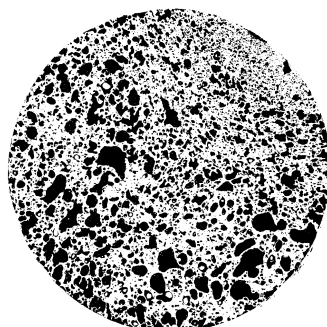
b005-01-B
(50102)
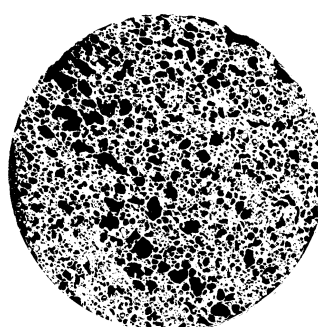
b006-01
(601)
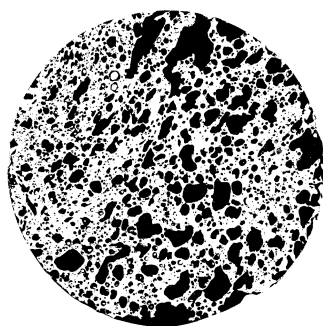
b007-01
(701)
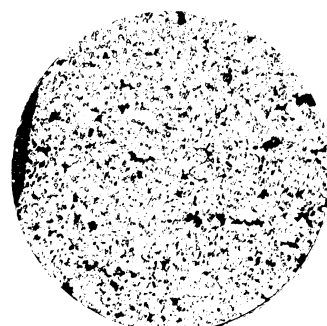
b010-01
(1001)

b013-01
(1301)
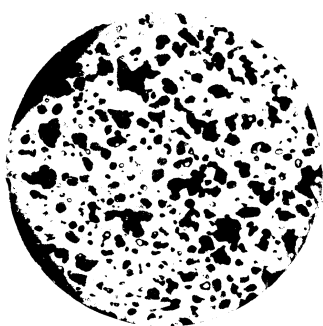
b014-01
(1401)
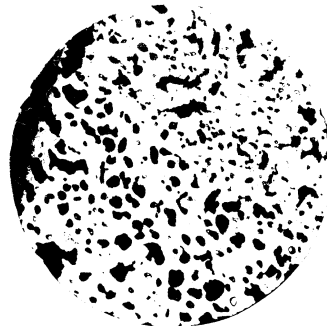
b014-02
(1402)
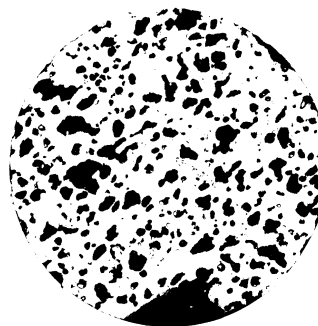
b014-04
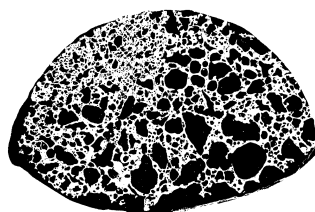(1404)
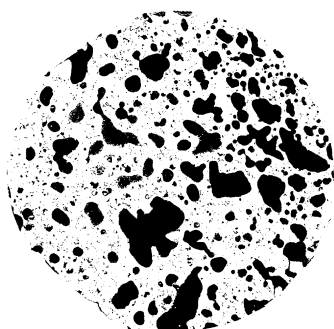
b016-01
(1601)
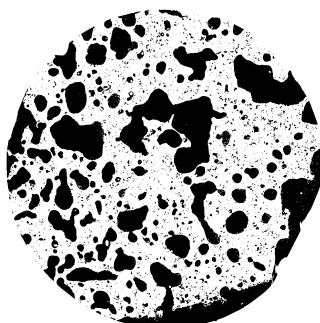
b016-02
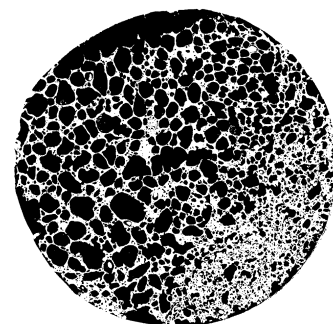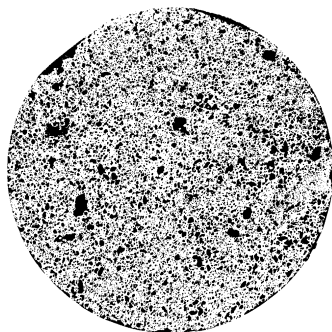(1602)
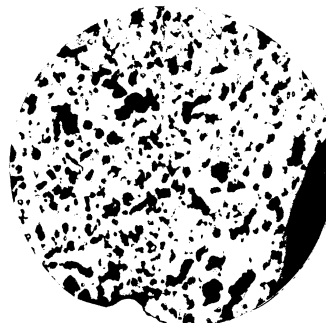
b019-02
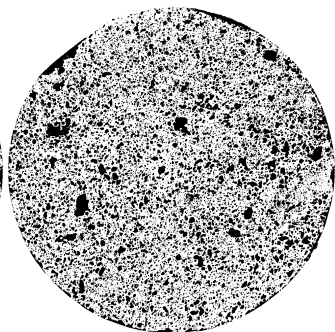(1902)
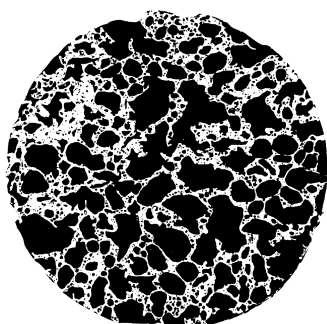
b020-01
(2001)
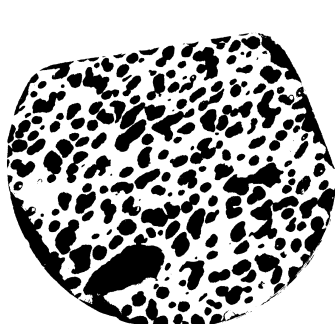
b02101-B
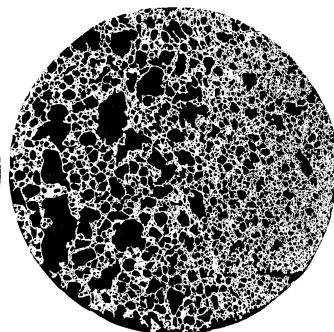(21012)
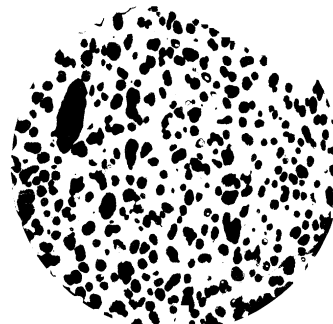
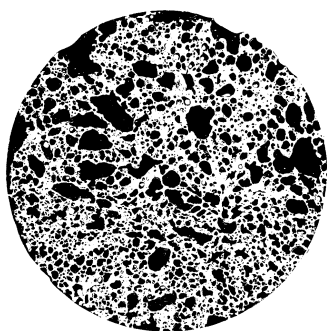b021-02
(2102)

b022-01
(2201)

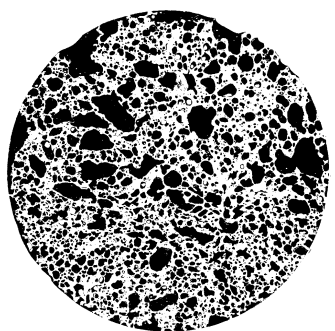b023-01
(2301)

b024-01
(2401)
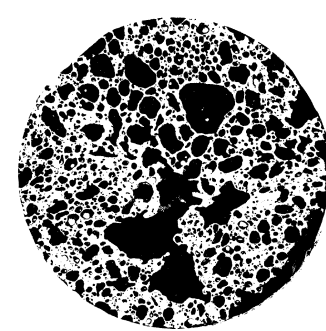
b025-01
(2501)

b025-02
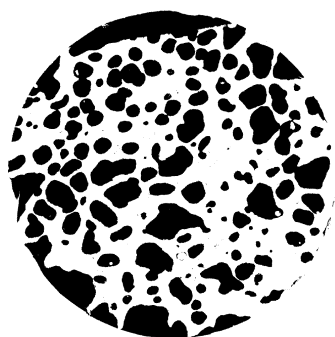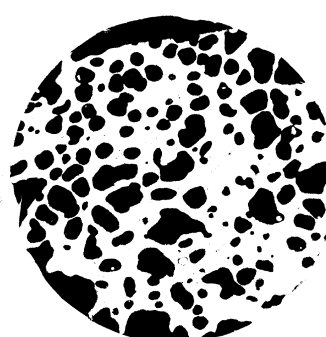(2502)
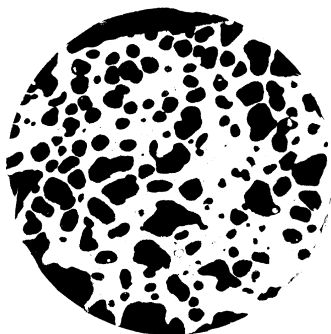
b026-01
(2601)
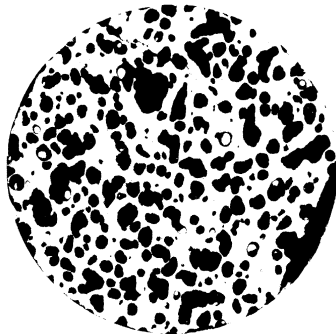
b028-01
(2801)

b02802
(2802)

b028-03
(2803)

b031-01
(3101)

b032-01
(3201)

b032-01-A
(320101)

b032-01-B
(320102)

b033-01
(3301)

b033-01-A
(330101)

Bibliography

ARCHIE, G.E. 1942 The electrical resistivity log as an aid in determining some reservoir characteristics. *Trans. Am. Inst. Min. Metall. Pet. Eng.* **146**, 54-62.

BAI, M. & ELSWORTH, D. & ROEGIERS, J.C. 1993 Multiporosity / multipermeability approach to the simulation of naturally fractured reservoirs. *Water Resour. Res.* **29**, 1621-1633.

BEAR, J. 1988 *Dynamics of Fluids in Porous Media.* Dover Publications Inc., New York.

BEAR, J. & TSANG, C.-F. & DE MARSILY, G. 1993 *Flow and Contaminant Transport in Fractured Rock.* Academic Press, San Diego, CA.

BERRYMAN, J.G. 1984 Measurement of spatial correlation functions using image processing techniques. *J. Appl. Phys.* **57**, 2374-2384.

BERRYMAN, J.G. & BLAIR, S.C. 1986 Use of digital image analysis to estimate fluid permeability of porous materials: application of two-point correlation functions. *J. Appl. Phys.* **60**, 1930-1938.

BERRYMAN, J.G. 1987 Relationship between specific surface area and spatial correlation functions for anisotropic porous media. *J. Math. Phys.* **28**, 244-245.

BERRYMAN, J.G. & BLAIR, S.C. 1987 Kozeny-Carman relations and image processing methods for estimating Darcys constant. *J. Appl. Phys.* **62**, 2221-2228.

BLACKWELL, D.D. & BAKER, S.L. 1988 Thermal analysis of the Austin and Breitenbush geothermal system, Western Cascades, Oregon. *Geology and Geothermal Resources of the Breitenbush-Austin Hot Springs Area, Clackamas and Marion Counties, Oregon*, 47-62. Oregon Dept. of Geology and Mineral Industries Open-File Report 0-88-5.

BLAIR, S.C. & BERGE, P.A. & BERRYMAN J.G. 1996 Using two-point correlation functions to characterize microgeometry and estimate permeabilities of sandstones and porous glass. *J. Geophys. Res.* **101** B9, 20,359-20,375.

BOSL, W.J. & DVORKIN, J. & NUR, A. 1998 A study of porosity and permeability using a lattice Boltzmann simulation. *Geophys. Res. Lett.* **25**, 1475-1478.

BOTTINGA, Y. & WEILL, D.F. 1972 The viscosity of magmatic silicate liquids: a model for calculation. *Am. J. Sci.*, **272**, 438-475.

BRACE, W.F. 1980 Permeability of crystalline and argillaceous rocks. *Int. J. Rock Mech. and Mining Sci. and Geomech. Abstr.* **17**, 241-251

CARMAN, P.C. 1956 *Flow of Gases Through Porous Media.* Academic Press, San Diego, CA.

CASHMAN, K.V. & MANGAN, M.T. & NEWMAN, S. 1994 Surface degassing and modifications to vesicle size distributions in active basalt flows. *J. Volc. and Geotherm. Res.* **61**, 45-68.

CLAUSER, C. 1992 Permeability of Crystalline Rocks. *EOS Trans. AGU* **73**, 233, 237-238.

CLOUD, W.F. 1941 *Oil Weekly* **103**, 26

CRISP, J. & CASHMAN, K.V. & BONINI, J.A. & HOUGEN, S.B. & PIERI, D.C. 1994 Crystallization history of the 1984 Mauna Loa lava flow. *J. Geophys. Res.* **99**, B4, 7177-7198.

DARCY, H. 1856 *Les Fontaines Publique de la Ville de Dijon.* Paris.

DICKINSON, W.R. 1965 Geology of the Suplee-Izee area, Crook, Grant, and Harney counties, Oregon. *Oregon Department of Geology and Mineral Industries. Bulletin* **58**, p.101

DULLIEN, F.A.L. 1979 *Porous Media - Fluid Transport and Pore Structure.* Academic Press, San Diego, CA.

FENG, S. & HALPERIN, B.I. & SEN, P.N. 1987 Transport properties of continuum systems near the percolation threshold. *Phys. Rev.* B **35**, 197-214.

FREEZE, R.A. & CHERRY, J.A. 1979 *Groundwater* Prentice-Hall, Englewood Cliffs.

GUÉGUEN, Y. & GAVRILENKO, P. & LE RAVALEC, M. 1996 Scales of rock permeability. *Surveys in Geophysics* **17**, 245-263.

INGEBRITSEN, S.E. & SCHOLL, M.A. 1993 The hydrology of Kilauea volcano. *Geothermics* **22**, 255-270.

JOHNSON, D.L. & KOPLIK, J. & SCHWARTZ, L.M. 1986 New pore-size parameter characterizing: transport in porous media. *Phys. Rev. Lett.* **20**, 2564-2567.

KATZ, A.J. & THOMPSON, A.H. 1986 Quantitative prediction of permeability in porous rock. *Phys. Rev.* B **34**, 8179-8181.

KENNEDY, M. R. & POZRIKIDIS, C. & SKALAK, R. 1993 Motion and deformation of liquid drops, and the rheology of dilute emulsions in simple shear flow. *Computers Fluids* **23**, 251-278.

KHITAROV, N.I. & LEBEDEV, YE.B. & DORFMAN, A.M. & BAGDASAROV, N.S. 1979 Effects of temperature, pressure and volatiles on the surface tension of molten basalt. *Geochem. Int.* **16**, 78-86.

KLUG, C. & CASHMAN K.V. 1996 Permeability development in vesiculating magmas: implications for fragmentation. *Bull. Volcanol*, **58**, 87-100.

LIPMAN, P.W. & BANKS, N.G. 1987 Aa flow dynamics, Mauna Loa 1984; Volcanism in Hawaii. *U.S. Geological Survey Professional Paper* 1527-1567.

MANGA, M. 1996 Hydrology of spring-dominated streams in the Oregon Cascades. *Water Resour. Res.* **32**, 2435-2439.

MANGA, M. 1997 A model for discharge in spring-dominated streams and implications for the transmissivity and recharge of quaternary volcanics in the Oregon Cascades. Water Resour. Res., **33**, 1813-1822.

MANGA, M. & CASTRO, J. & CASHMAN, K.V. & LOEWENBERG, M. 1998 Rheology of bubble-bearing magmas: theoretical results. submitted to *J. Volc. and Geotherm. Res.*

MANGAN, M.T. & CASHMAN, K.V. & NEWMAN, S. 1993 Vesiculation of basaltic magma during eruption. *Geology*, **21**, 157-160.

MANGAN, M.T. & CASHMAN, K.V. 1996 The structure of basaltic scoria and reticulite and inferences for vesiculation, foam formation, and fragmentation in lava fountains. *J. Volc. and Geotherm. Res.* **73**, 1-18.

MIYAZIMA, S. 1987 Percolation transport exponents in a generalized swiss-cheese model and a generalized inverted swiss cheese model for a conductive substance. *J. of the*

Phys. Soc. of Japan, Lett. **56**, 1268-1270.

PATERSON, M.S. 1983 The equivalent channel model for permeability and resistivity in fluid-saturated rock – A re-appraisal. *Mech. Mater.*, 345-352.

PHILLIPS, F.R.S. 1991 *Flow and Reactions in Permeable Rocks.* Cambridge University Press, NY.

POLACCI, M. & PAPALE, P. 1997 The evolution of lava flows from ephemeral vents at Mount Etna: insights from vesicle distribution and morphological studies. *J. Volc. and Geotherm. Res.* **76**, 1-17.

POLACCI, M.S. & CASHMAN, K.V. 1998 submitted to *Bull. Volc.*

ROBERTS, J.J. & BERGE, P.A. & CARLBERG, E.D. 1997 Comparison of laboratory, analytical, and imaging techniques for estimating permeability in porous media. submitted to *Water Resour. Res.*.

ROSE, H.E. 1945 *Proc. Inst. Mech. Eng. Appl. Mech.* **153**, 141.

SAHIMI, M. 1994 *Applications of Percolation Theory.* Taylor & Francis, London, Bristol, PA.

SAHIMI, M. 1995 *Flow and Transport in Porous Media and Fractured Rock.* VCH Verlagsgesellschaft mbH, Weinheim, Germany.

SÁNCHEZ-VILA, X. & CARRERA, J. & GIRARDI, J.P. 1996 Scale effects in transmissivity. *J. of Hydrology* **183**, 1-22.

SANFORD, W.E. 1997 Correcting for diffusion in carbon-14 dating of ground water. *Groundwater* **35**, 357-361

SEN, P.N. & SCALA, C. & COHEN, M.H. 1981 A self-similar model for sedimentary rocks with application to the dielectric constant of fused glass beads. *Geophysics* **46**, 781-795.

STAUFFER, D. 1985 *Introduction to Percolation Theory.* Taylor & Francis, London, Bristol, PA.

TAYLOR, G.I. 1932 The viscosity of a fluid containing small drops of another fluid. *Proc. R. Soc. Lond.* A, **138**, 41-48.

TIDWELL, V.C. & WILSON, J.L. 1997 Laboratory method for investigating permeability upscaling. *Water Resour. Res.* **33**, 1607-1616.

TIPLER, P.A. 1991 *Physik* Spektrum Akademischer Verlag, 3. edition

WALKER, D. & MULLINS JR., O. 1981 Surface tension of natural silicate melts from 1200°-1500° and implications for melt structure. *Contrib. Mineral. Petrol.* **76**, 455-462.

WALKER, G.W. & MACLEOD, N.S. 1991 *Geologic Map of Oregon, scale 1:500,000* U.S. Geological Survey

WALSH, J.B. & BRACE, W.F. 1984 The effect of pressure on porosity and the transport properties of rock. *J. Geophys. Res.* **89**, 9425-9431.

WILLIAMS, J.A. & SOROOS, R.L. 1973 Evaluation of methods of pumping test analysis for application to Hawaiian aquifers. *Water Resour. Res. Center, Tech. Report 20, University of Hawaii, Honolulu,* 159 pp.

WONG, P.Z. & KOPLIK J. & TOMANIC J.P. 1984 Conductivity and permeability of rocks. *Phys. Rev.* B **30**, 6606-6614.